2019

Formation of O2 From CO2 Ice Photolysis

Christina Buffo
Wellesley College, cbuffo@wellesley.edu

Formation of O_2 From CO_2 Ice Photolysis

Christina E. Buffo

Submitted in Partial Fulfillment

of the

Prerequisite for Honors

in Chemical Physics

under the advisement of Karin Öberg

(Harvard Center for Astrophysics)

and Chris Arumainayagam

April 2019

Acknowledgements

First, thank you to Professor Chris Arumainayagam for four years of support and encouragement. Without your guidance, advice, and frequent emails, I never could have made it this far. Thank you for believing in me.

Sincere thanks to Dr. Karin Öberg for your incredible patience and insightful advice on everything from grad school applications to proper graph formatting. Throughout the year and especially as the deadline draws ever closer, thank you for your clear explanations and detailed feedback. Many thanks to Dr. Mahesh Rajappan for troubleshooting guidance, training me on SPACECAT, and maintaining an amazingly well-organized lab environment.

Thanks to my committee members, Professors Rachel Stanley and James Battat, for your patience with scheduling and your useful comments that have helped me conceptualize how this work fits with the rest of the field. Thank you to Professors Yue Hu and Megan Núñez for working around last-minute scheduling constraints, and to Professor Richard French for agreeing to serve as my honors visitor.

Thank you to all past and present Arumainayagam lab members for teaching me ultrahigh vacuum skills, general experiment-running practices, and how not to lose your mind as a thesising student.

A heartfelt thank you to all of my friends for putting up with me. Thank you to my many chemistry and physics friends for the many hours we have spent psetting. Thanks and congratulations to fellow thesising students - we made it! Thank you to my Wellesley Wushu family, past and present, who have given me a home here on campus, supported me through rough times, and helped me celebrate everything from learning new sword techniques to finding the next steps on my path forwards. Thank you especially to Jo Sehon, Laura Scanlon, Phoebe Amory, Sara Cooper, and Vivian Yu for being the strangest, most understanding, and most fun floormates possible.

Special thanks to Chloe Shi and Emily Jin for more things than I could possibly say. Chloe, through all the time we spent planning a show, dramatically lipsyncing to emo music, and just existing, I am always grateful for you. Emily, you have been the older sister figure I never knew I needed. You two have defined so much of my Wellesley life and helped me grow, and I will always appreciate you.

Last and certainly not least, thank you and love to my family. Thank you Mom and Dad for your enthusiastic support and always checking in, especially when the future is uncertain. You encouraged my interest in science since I was a small child obsessed with the moon, and have always believed in me. Matthew, thank you for being a fantastic younger brother and co-conspirator. I hope I can make you all proud!

1 Abstract

The recent *Rosetta* and *Giotto* missions to comets have detected the presence of a surprisingly large amount of O_2 within cometary comae [5] [43]. Most comet formation models suggest that comet compositions preserve conditions in the early solar system [34], so one possible origin of this diatomic oxygen is formation within ice layers on small dust particles in space before or during solar system formation. One common ice component is carbon dioxide, and this thesis focuses on O_2 formation from UV photolysis of CO_2 ices. Viewed in the context of the evolution of related molecules, CO and O_3, we examine O_2 production as a function of UV photon fluence and ice temperature. We report that the ideal conditions for O_2 production are a large photon fluence and ice temperatures in the range of 20-25 K, which are reasonable conditions for the interstellar medium [18]. In light of these findings, we propose that interstellar regions with significant CO_2 ice could partially explain the large abundance of O_2 in comets.

2 Introduction

For thousands of years, people across the world have observed comets and wondered about these "stars" with stunningly long tails. In the past hundred years, as technological developments made sending missions to comets possible, they are no longer viewed as potential harbingers of doom, but many cometary mysteries remain. Two missions have found the unexpectedly substantial presence of diatomic oxygen, O_2, on comets 1P/Halley and 67P/Churuymov-Gerasimenko (67P/C-G) [5] [43]. In this paper, I investigate one potential pathway for O_2 formation: UV irradiation of CO_2 ices.

Diatomic oxygen has been the focus of many investigations in astronomy, including in astrobiology-focused studies. Outside our solar system, efforts for finding life on other planets have included looking for O_2 in extrasolar planet transit spectra [37]. On a planet, significant amounts of free gaseous O_2 have the potential to be a false positive but seem to be a reasonably promising biomarker [37] [35]. A possible abiotic formation mechanism is UV photolysis of water, but on earth, this process accounts for less than 1% of O_2 production [37]. The lack of a dipole moment of O_2 and its resulting IR invisibility makes ozone, O_3, a useful remote detection proxy [37] in the search for life.

Within the solar system, both solid and gaseous O_2 have been detected in a variety of environments. Optical-reflectance measurements revealed the presence of solid oxygen on Ganymede, one of Jupiter's icy moons [47] [49] [2]. The presence of IR absorption lines of O_3 within these ice layers suggests that this oxygen likely comes from radiolysis of water ice. Rhea and Dione, two of Saturn's moons, also have O_3 ices, which is thought to result from reactions of diatomic oxygen [40]. In support of this theory, the Cassini Plasma Spectrometer (CAPS) and Ion Neutral Mass Spectrometer (INMS) also detected O_2^+, a potential reaction intermediate, within Saturn's icy rings [28].

Earth is not the only body in the solar system with gaseous O_2 in its atmosphere. Complex photochemistry in the Martian atmosphere produces trace amounts of gaseous O_2 [3] [34]. Some moons also have O_2 in their atmospheres: Cassini INMS detected a tenuous O_2 and CO_2 atmosphere on Rhea [51]. Europa also has a flimsy gaseous diatomic oxygen atmosphere, which was confirmed by Hubble's Goddard High Resolution Spectrograph (GHRS) [22].

However, all these environments have undergone significant changes in physical structure, temperature, relative abundance of various compounds, and other properties since the early solar system. Environmental alterations would allow a variety of oxygen-forming pathways to occur, including O_2 production by living organisms. Comets, whose compositions and histories are very different from planets and moons, were not anticipated to have significant amounts of O_2.

2.1 Comet Background

Comets consist of ice grains and dust particles, though the specific ratio of ice to dust and the particular chemical composition may vary. Comets can be grouped based on their orbital period and farthest distance from the sun, or aphelion. Periodic comets have orbital periods of less than 200 years, and aphelion distances within the Kuiper Belt, which reaches distances of about 50 astronomical units (AU), the distance from Earth to the sun. Long-period comets take much longer to orbit the sun, and can often only be observed once during their rare approach into the inner solar system. The "dirty snowball" or "snowy dirtball" core of the comet is the nucleus. When the comet nears its perihelion distance, or closest approach to the sun, some of its ice sublimates and forms a fuzzy, cloud-like gas and dust halo around the nucleus, called the coma [6]. The bright and easily visible main tail of the

comet results from dust particles being carried away from the comet by solar radiation.

Comet formation models show several origin possibilities. Most theorists agree that they developed from accumulating clumps of gas and dust during solar system formation from the slowly spinning disk of matter, or protoplanetary disk. Some models suggest that comets have remained at approximately the same distance from the sun since they formed. Others hypothesize that they could have been ejected from the range of the gas giants, while one model even proposes that the sun captured many comets from sibling stars forming at the same time [39].

Regardless of their exact formation location, the process seems to be largely the same: millimeter to centimeter sized clumps of dust stick to each other to form meter-sized boulders [54]. These boulders then can collect in gravitational instability pockets in the protoplanetary disk, eventually acquiring enough mass to gravitationally collapse and form an spheroid, kilometer-sized object, called a planetesimal [6]. Some planetesimals eventually collide and combine to form planets, but others remain separate and likely become comets. The majority of these remaining planetesimals have sizes between tens of meters and one kilometer [54]. The location of the snow line, or minimum distance from the star for water ices to form, partially determines a planetesimal's fate. Outside this radius, the dominant material is water ice. Models suggest that the average temperature in this region never reaches the melting point of water ice, so ices from before solar system formation could be preserved [27]. Planetesimals that form in this region are more likely to grow to larger masses and "fluffier" structures [6] that consist of a mixture of ice and dust with a "rubble pile"-like structure and the potential for significant internal variation [27].

What does the ice in these proto-comets look like? Much of this ice formed before the solar system from the "natal interstellar cloud core" [39], an interstellar cloud of gas and dust. After ice incorporation into comets, it may be preserved with very little modification. Alternatively, it may be completely destroyed and reformed, or processed to a lesser or greater degree by ice processes occurring within the protosolar disk, which include thermochemistry, photochemistry, and radiation chemistry from incident cosmic rays. Degrees of processing may vary by comet location and even within ices of the same comet [26] [39]. Despite the presence of these processes within proto-comets, other planetesimals that later become asteroids, planets, or other solar system objects typically experience far more drastic

transformations. Therefore, comets are still largely considered some of the least modified objects in the solar system [39] [54] [34]. An improved understanding of their composition may reveal not only the conditions of the protostellar nebula (PSN), but potentially also those of the ISM.

2.2 *Rosetta* and *Giotto* Mission Findings

In light of the theories that cometary ice would have largely been preserved from the early solar system, the results from the European Space Agency's *Rosetta* and *Giotto* missions were surprising. Prior to these missions, comets were theorized to have very low amounts of molecular diatomic oxygen because of its reactivity and its low observed abundance in the ISM and protoplanetary disks. However, the *Rosetta* mission's Double Focusing Mass Spectrometer (ROSINA/DFMS) measured a O_2 concentration of 1-10 % relative to water in the coma of comet 67P/Churyumov-Gerasimenko (67P/C-G). The DMFS mean concentration value of 3.80 ± 0.85 % [5] was confirmed by the Alice ultraviolet (UV) imaging spectrograph, which measured a mean relative column abundance of 25 % relative to water [29] [15]. Both of these detection methods suggested that the O_2 originated from sublimating ice, because 67P/C-G passed through its perihelion distance while *Rosetta* was in orbit, and the temperatures became high enough to cause substantial ice sublimation. A review of data collected by the Neutral Mass Spectrometer (NMS) of the European Space Agency's *Giotto* flyby of comet 1P/Halley indicated similarly high concentrations of O_2 relative to water in the coma [43] [5].

This similarly high abundance of O_2 may be the result of similar origins of these two comets. However, present orbit differences may mean their formation conditions were very different. Comet 67P/C-G has an orbit within the inner solar system, from inside the orbit of Mars to just outside the orbit of Jupiter, while comet 1P/Halley travels outside the orbit of Pluto. If these two comets did have different formation conditions, similarly high O_2 levels may instead point to efficient oxygen formation throughout the protosolar nebula and interstellar medium.

2.3 Molecule Formation in the Interstellar Medium

In order to understand why comet ices contain molecular oxygen, we must take a step back to look at molecule formation prior ice accumulation. Molecules form in three phases in the interstellar medium:

in the gas, on the surfaces of dust grains, and inside of ice layers on dust grains. Molecules formed in any of these locations could end up being frozen in ices, due to efficient condensation into ice in many interstellar cloud regions.

Within the gas phase, most reactions are binary collisions between molecules, which are frequently exothermic and have no or very low activation energies [23]. Because the most common molecule is H_2 [23] and ion-molecule reactions frequently do not have activation energy barriers, many gas phase reactions are considered to be between H_2 and an ion. Most of the chemistry that could impact comet compositions occurs in interstellar over-densities or clouds that are considered "dark", with no light penetration. The only outside radiation is cosmic rays, which can ionize molecules to produce free electrons and cations, and produce secondary, weak UV fields. The gas phase elements are hydrogen, helium, carbon, nitrogen, and oxygen. Diatomic oxygen could form in the gas phase from reactions of free oxygen atoms with OH:

$$O + OH \rightarrow O_2 + H \tag{1}$$

This gas phase O_2 could later freeze into ices [23].

The second potential location for molecule formation is on the surface of interstellar dust grains. Graphite and silicates are the most common components of dust grains [52], and molecules frequently found on particle surfaces include water, carbon monoxide, and carbon dioxide [52]. Free atoms, such as H, C, and O, as well as small molecules like H_2, can move over the grain surface and react with other atoms. Diatomic oxygen could potentially form through such a pathway, or from reactions of oxygen-containing molecules on a surface, but it could also be consumed through similar reaction avenues [52]. Examples of these reactions include the production of O_2 from O_3:

$$H + O_3 \rightarrow O_2 + OH \tag{2}$$

This newly formed O_2 could be destroyed through reactions with H atoms:

$$H + O_2 \rightarrow HO_2 \tag{3}$$

These sorts of reactions would require warmer and denser conditions than those typically found in the interstellar medium [50].

Ice-phase reactions, the focus of this thesis, can occur in any type of ice, both "pure" ices containing predominantly one species and "mixed" ices with a variety of compounds. In general, ice phase reactions typically occur when some form of radiation incident on ice excites, ionizes, and/or breaks apart molecules. These molecules or fragments can then react with other molecules within the ice layers or on ice surfaces [57]. Irradiation of any oxygen-containing ices could theoretically produce O_2. H_2O, CO, and CO_2 are some of the most common oxygen-containing molecules in the interstellar medium [39], so large amounts of ice-phase O_2 likely form from irradiation of ices of one or more of these molecules.

2.4 O_2 Formation and Abundances in Astrochemical Environments

To put cometary oxygen into context, it is useful to consider O_2 abundances in the different stages of star and planet formation. Atomic oxygen, O, is the third most abundant element in the universe [34], after hydrogen and helium. However, the presence or absence of O_2 in different environments has been notoriously difficult to verify. Due to its lack of a permanent dipole moment, it was long unclear whether the scarcity of detections was due to insufficient instrument sensitivity or if O_2 does not actually exist in space with a significant abundance. Outside the solar system, vibrational transitions of gas phase O_2 have been detected in only a few clouds in the ISM, with infrared (IR) telescopes [11]. The first such cloud with a confirmed detection was the ρ Ophicus A molecular cloud [31], where O_2 was detected first by the IR detector on the *Odin* satellite. This identification was later confirmed by the *Submillimeter Wave Astronomy Satellite (SWAS)* telescope [48], the *Spitzer Space Telescope* [30], and the *Herschel* space telescope [33]. Gaseous O_2 has also been detected in the Orion interstellar cloud [21] [10] by *Herschel*, but both locations show very low concentrations of O_2 relative to H_2.

Solid phase O_2 has not yet been detected in interstellar grains, but has been suggested to act as a reservoir for molecular oxygen [1] [14]. Efforts to observe solid phase O_2 have included searching for its fundamental vibration lines around 1550 cm^{-1} in protostellar locations [34] [1].

One proposed ISM formation route is interactions between high energy radiation and H_2O ices to

form O_2. Incident photons, cosmic rays, or electrons could cause H_2O photolysis or radiolysis, and explain the correlation in signals of O_2 and H_2O detected by *Rosetta* [5].

Once the protosolar nebula started forming, O_2 previously in the gas phase could become trapped in ices. This process would require rapid temperature changes, which do occur in the early solar system [50] [5]. However, such rapid temperature changes would also cause molecules with similar freezing points, such as gaseous CO and N_2, to condense into ice at the same time. Since the resulting ices would likely be mixed, evaporation of these ices would result in correlations between CO and H_2O, and N_2 and H_2O in comet outgassing. These trends were not seen with either *Rosetta* or *Giotto*, casting doubt on this theory. Alternatively, gaseous O_2 could become trapped in clathrates, a different form of solid water [38]. This scenario would produce a strong correlation between O_2 and CO and/or CO_2 [34], which is not seen in 67P/C-G. A third possibility for O_2 formation during comet formation is radiolysis of water in icy grains cycled between the cooler, darker, ice-forming midplane of the protostellar disk and the warmer upper disk layers, which are exposed to a higher flux of energetic galactic cosmic rays [38]. However, the timescale required to form and trap O_2 in the abundances observed in comets would exceed the likely timescale required to form a comet [34].

If substantial amounts of diatomic oxygen did not form in the interstellar medium or protosolar nebula, O_2 could be currently forming within the comet itself. Products of past radiolysis or photolysis in the upper few centimeters of cometary ice layers would have evaporated in the warmer temperature of the inner solar system, and would not have been detected by *Rosetta*. Current radiolysis or photolysis of surface comet ices would show a variable ratio of O_2/H_2O due to changing illumination during the several months of the *Rosetta* observation period, which is not seen [5]. While the fluctuations in exact amounts of O_2 and H_2O detected vary depending on the amount of sunlight different sections of the comet receive, only small variations in the ratio are observed [5]. This suggests that the majority of O_2 has already formed within the ice prior to incorporation into the comet. Other, non-ice formation possibilities include dismutation of gas phase H_2O_2 in the coma of a comet [13], or radiolysis by radioactive nuclei in the comet itself (endogenic radiolysis) [8]. Eley-Rideal reactions, in which one reactant is in the gas phase and the other is attached to a surface, have also been proposed [56], but more recent studies have indicated that these reactions will not produce O_2 in the observed quantities

[24].

To summarize the diatomic oxygen formation prospects listed so far, cometary O_2 could have formed either before or after comet formation. Before the solar system existed, diatomic oxygen could be produced through gas phase, grain surface phase, or ice phase reactions. Ice phase sources of oxygen include H_2O, CO_2, and CO, three common oxygen-containing molecules in the interstellar medium [46] [39]. All of these production possibilities could have resulted in significant amounts of O_2 remaining preserved in cometary ices. The other category of possible formation methods consists of reactions currently happening within the comet. This category includes photolysis and radiolysis of cometary ice, fragmentation of H_2O_2 within the coma of the comet, and Eley-Rideal reactions.

2.5 CO_2 in Astrochemical Environments

In this thesis, I focus on a different pathway for O_2 formation: UV irradiation of CO_2 ice.

Outside the solar system, carbon dioxide is a very common molecule. Carbon monoxide, CO, and carbon dioxide, CO_2, are some of the most abundant molecules in the interstellar medium, with a maximum abundance of ≈ 50 % relative to water [12] [36] [39] [55]. CO_2 has been observed in many locations and stages of star formation. Like O_2, CO_2 cannot be detected with rotational spectroscopy in far-infrared or submillimeter wavelengths because of its lack of a permanent dipole. Infrared observations of vibrational transitions from Earth are not possible because of high levels of CO_2 in Earth's atmosphere [7]. Satellite telescopes such as the *Infrared Space Observatory* [20] and *Spitzer* have observed IR CO_2 vibrational bands [42] [45], and the next generation of IR instruments on board the *James Webb Space Telescope* will be even more sensitive [19]. Related gaseous species, such as HCO_2^+, have also been detected in the interstellar medium, suggesting that CO_2 chemistry actively occurs [44] [53].

Most interstellar CO_2 is mixed with H_2O ice, but for simplicity in modeling, this thesis focuses solely on pure CO_2 ice. Pure solid amorphous CO_2 ice, like the ice used in this thesis, has also been observed in small quantities, as has pure solid crystalline CO_2 ice [16]. Such ice may form as a result of evaporation of CO from mixed CO and CO_2 ice [36] [42].

Within comets, CO_2 is also one of the most abundant species, after water and CO [5] [34]. Sig-

nificant CO_2 outgassing from comet 67P/C-G and comet 1P/Halley has been detected. One common method of estimating frozen CO_2 abundance is comparing the red and green emission lines of excited oxygen atoms, which have been recently shown to also be sensitive to O_2 concentrations [9]. Previous predictions of CO_2 and O_2 abundances would therefore overestimate CO_2 and underestimate O_2. A better understanding of this relationship provides another motivation for studying the dynamics between CO_2 and O_2 formation. In comets, the CO_2 ice appears partially segregated from the main water ice reservoir, so reactions within pure CO_2 ice may occur [41].

2.6 Previous Studies of O_2 Formation in CO_2 Ice

O_2 production from CO_2 photolysis has been previously studied in the laboratory. Like the experiments detailed in this thesis, some monitor photoproduct formation both during irradiation and final product yield [36]. One study found an upper limit of O_2 yield of 38% relative to the initial CO_2 from post-irradiation temperature-programmed desorption (TPD) experiments, but did not specify a lower limit. O_3 and CO evolution were also monitored through infrared (IR) spectroscopy during irradiation: significant CO production was found, but only trace amounts of O_3 [36]. Based on the TPD and IR results, this study proposed a network of reactions for photoproduct formation and destruction, which we will also adopt: photolysis of CO_2 to form CO and O results in the presence of free O atoms, which can combine to form O_2. Additional free O atoms can also combine with O_2 to form O_3. Also, this study found that the majority of the photoproducts remained trapped in the CO_2 ice rather than being ejected by irradiation (photodesorption). This conclusion adds support to the idea that O_2 could remain trapped in parent CO_2 ice.

2.7 This Thesis

In this thesis, I build off of previous work of CO_2 irradiation by UV light [36] to characterize the O_2 formation efficiency and formation mechanism. Since O_2 cannot be observed with a laboratory infrared spectrometer, I instead follow CO and O_3 production during irradiation. After UV irradiation, temperature programmed desorption (TPD) data are collected for CO_2, CO, O_2, O_3, and their fragments. Section 3 describes the experimental details.

A description of the CO_2 photolysis experimental parameters is given in Section 4. Section 5 focuses on O_2 formation yields after different irradiation doses, and at different ice temperatures. To put O_2 formation in the context of other reactions happening within the ice, Section 6 of this thesis looks at CO and O_3 formation during irradiation. Section 7 examines CO and O_3 formation kinetics and their implications for O_2 production. In Section 8, I discuss the experimental results and propose a mechanism that is guided by observed photoproduct formation patterns.

3 Experimental

3.1 Experimental Setup

The experiments were carried out in a laboratory setup designed for the study of interstellar ices, described in more detail previously by Lauck et al (2015) [32]. All experiments were conducted within a spherical stainless steel ultrahigh vacuum (UHV) chamber, which is pumped to a base pressure of approximately 10^{-10} torr by a Pfeiffer Turbo HiPace 400 pump and a DUO 10 M rotary vane pump. Ices are created by deposition of 99.9 % isotopically pure $^{12}CO_2$ (Sigma-Aldrich) through a gas line and precision leak valve onto an IR transparent CsI crystal. This CsI crystal is capable of 360-degree rotation, allowing both ice deposition and UV irradiation to occur normal to the surface. The temperature of the surface, and of the ice that forms on it, is monitored and maintained by a temperature controller (LakeShore 335) and a closed-cycle He cryostat (ARS-4HW Compressor). These temperature measurements have an accuracy of 2 K and a relative uncertainty of 0.1 K. During gas dosing and ice formation, the thickness of the ice is measured with IR transmission spectra (see Section 3.2 on IR column densities). Recent investigations have revealed a potential problem with absolute thickness calibration due to issues with IR design or optics within the chamber, so the absolute thickness calibration may be inaccurate. Relative error between experiments should be small.

Following dosing of the ice, measurements of infrared-active molecules within the ice are taken with a Fourier transform infrared spectrometer (Bruker Vertex 70v) in transmission mode. The ice was irradiated with ultraviolet (UV) light from an H_2D_2 lamp (Hamamatsu H_2D_2 Light Source L11798), whose spectral distribution was shown with greater detail previously in Bergner et al (2017) [4]. A

NIST calibrated AXUV-100G photodiode was used to measure the photon flux from the UV lamp, which fell in the range of approximately 10^{13} photons second^{-1} cm^{-2} (see Table 3).

During irradiation, the IR spectrometer monitored from 4000 to 800 wavenumbers. The key frequencies monitored corresponded to CO_2, CO, and O_3, as listed in Table 1.

Following irradiation, temperature-programmed desorption (TPD) data were collected, during which the temperature controller increased the ice temperature at a rate of 2 K per minute, from the irradiation temperature up to 150 K. A quadrupole mass spectrometer (Pfeiffer PrismaPlus Quadrupole QMG 220M1) (QMS) was used to observe the final products during the TPD, and the masses monitored are listed in Table 2. The masses monitored correspond to the main photoproducts and their fragments, and H_2O as a potential vacuum contaminant. All fitting and analysis is done using personal python scripts and the *matplotlib* package [25].

Molecule	Frequency (cm^{-1})	Band strength (cm molecule^{-1})
CO_2	2344	7.6×10^{-17}
CO	2141	1.1×10^{-17}
O_3	1042	1.4×10^{-17}

Table 1: IR band strengths used to calculate the column density of each component, which are assumed constant over temperature range measured. From Martín-Doménech (2015) [36].

Species	Mass Monitored (m/z)
^{12}C	12
^{16}O	16
H_2O	18
CO	28
O_2	32
CO_2	44
O_3	48

Table 2: Masses monitored by the quadrupole mass spectrometer (QMS) throughout a CO_2 photolysis experiment.

3.2 IR Spectra Column Densities

For all three IR-active species - CO_2, CO, and O_3 - the following equation is used to quantify the number of monolayers:

$$N_i = \frac{\int \tau_i(\nu) d\nu}{A_i} \tag{4}$$

In Equation 4, N_i is the column density (molecule cm^{-2}), $\int \tau_i(\nu) d\nu$ is the integrated optical depth of the IR band area (absorbance units), and A_i is the band strength of the relevant species in optical depth units [32]. Relevant column densities and wavelength positions are listed in Table 1. During irradiation, IR spectra are typically taken every five minutes (every 10 minutes during experiment 14): each spectrum is averaged over 64 interferograms and takes approximately 1 minute to complete. In all IR figures shown, a local baseline is fit to the area around the relevant peak. The number of monolayers (ML) for every species is calculated with the typical approximation of 1 ML = 10^{15} molecules cm^{-2} [4].

3.3 O_2 Quantification

Because O_2 is not infrared active, determination of O_2 production in the ice is based on mass spectrometeric measurements during the TPD, similar to Fayolle et al 2016 [17]. To determine the TPD signal corresponding to one monolayer, we first create water ice and then dose different amounts of O_2 on the surface. Because of the different energies of O_2 - O_2 and O_2 - H_2O interactions, the surface molecules of O_2 will desorb at different times during a TPD.

In order to interpret the TPD data, we must introduce some TPD theory. The rate of molecule desorption is given by the Polyani-Wigner equation:

$$-\frac{d\theta}{dT} = \frac{\nu}{\beta}\theta^n e^{-E_{des}/T} \tag{5}$$

In the above equation, θ is the ice coverage, T is the temperature in K, ν is a pre-exponential factor in s^{-1}, β is the heating rate in K s^{-1}, n is the desorption order, and E_{des} is the desorption energy in K [17]. For completeness, the pre-exponential factor associated with O_2 is the harmonic oscillator

approximation:

$$\nu = \sqrt{\frac{2n_s E_{des}}{\pi^2 m}} \tag{6}$$

In this equation, E_{des} corresponds to the same desorption energy as in Equation 5, n_s is the number of binding sites ($\approx 10^{19}$ sites m^{-2}), and m is the mass of the molecule in kg [17]. This expression for ν is provided for reference: precise formulation of the numerical values of all parameters in the Polyani-Wigner equation is necessary to determine desorption energies, but does not apply to calculations of total number of desorbed molecules.

For our purposes, the focus is determining the TPD integrated signal corresponding to approximately one monolayer, or 10^{15} molecules of O_2. The primary importance of these equations is the value of n in Equation 5, which allows distinguishing between the monolayer and multilayer regimes. The multilayer regime, corresponding to O_2-O_2 interactions, is considered a zeroth-order desorption process where $n = 0$ in Equation 5. Where O_2 interacts with the H_2O substrate, the submonolayer regime, desorption is a first-order process with $n = 1$ in Equation 5. These two desorption regimes can be distinguished because O_2 - O_2 interactions are weaker than O_2 - H_2O interactions. This results in O_2 desorption from the mulitlayer regime occurring at lower temperatures than O_2 from the submonolayer regime. Additionally, zeroth and first order desorption result in different TPD shapes.

The O_2 film thickness corresponding to one monolayer should have a small but visible zeroeth order multilayer peak in addition to the more prominent first order monolayer peak, since these thin ices are never perfectly flat. For comparison, a much larger O_2 dose would have a very prominent multilayer peak and a nearly-invisible monolayer peak, because the vast majority of O_2 molecules would only interact with other O_2 molecules. For a significantly smaller O_2 dose, with O_2 molecules directly on the water substrate and minimal O_2-O_2 interactions, only a monolayer peak would be present.

The experimental procedure for these O_2 TPD experiments first requires the creation of a water ice substrate: deionized water, purified through at least three freeze-pump-thaw cycles using liquid nitrogen, was deposited on the CsI crystal. This substrate had a film thickness corresponding to approximately 100 ML, as determined by IR measurements. During water deposition, the crystal tem-

perature was maintained at 100 K to grow compact water ice substrates. Following water deposition, the water ice was cooled to 20 K, and then 99.9 % $^{16}O_2$ (Sigma-Aldrich) was deposited through a gas handling line onto its surface. A temperature-programmed desorption experiment was then conducted, heating the ice at a temperature rate of 2 K per minute from 20 K to 100 K.

Number	Dose Time	Integrated Area	Monolayer Estimate
1	5 min	1.3×10^{-7}	Multilayer
2	2 min	6.0×10^{-8}	Multilayer
3	1 min 30 sec	3.0×10^{-8}	Monolayer
4	1 min	2.8×10^{-8}	Submonolayer
5	45 sec	1.8×10^{-8}	Submonolayer
6	30 sec	1.3×10^{-8}	Submonolayer

Table 3: Dose times, integrated area, and monolayer estimate for all O_2 TPD experiments.

Table 3 lists the parameters of the O_2 TPD experiments used to determine the QMS integrated area corresponding to one monolayer.

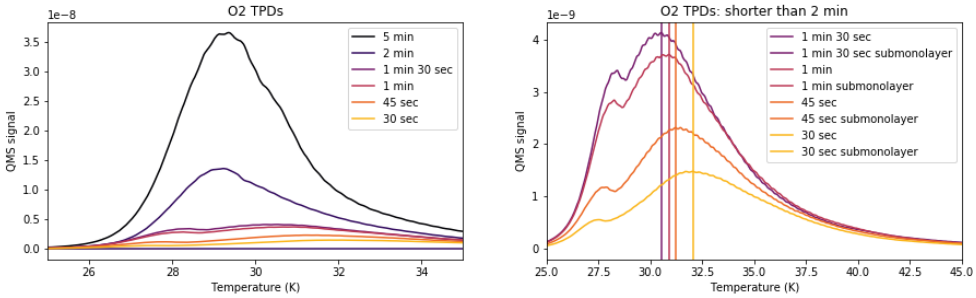

Figure 1: Left: O_2 (m/z 32) QMS signal during a temperature-programmed desorption experiment for dose times of 5 minutes, 2 minutes, 1 minute 30 seconds, 1 minute, 45 seconds, and 30 seconds. Right: The results from the same 1 minute 30 seconds, 1 minute, 45 seconds, and 30 second dose times. These four experiments all show two peaks in the O_2 signal, with the lower temperature signal at around 28 K corresponding to the multilayer peak and the higher temperature signal at approximately 31 K representing the monolayer peak. Because the 1 minute 30 second signal is the largest with clear monolayer and multilayer peaks, we take its integrated area to be approximately one monolayer.

Figure 1 shows the TPD results of several O_2 doses with different times. The four shortest dose times, plotted in the right panel of Figure 1, show two distinct peaks in the O_2 signal: one at approximately 28 K and one at approximately 31 K. Because of its smaller relative size and lower temperature, the peak at around 28 K corresponds to the multilayer regime. The higher temperature peak at approx-

imately 31 K corresponds to the zeroth-order submonolayer regime. Because the integrated area of the monolayer peak should have both multilayer and submonolayer regimes, we take the integrated area of the monolayer peak from the 1 minute 30 second dose to be approximately equal to one monolayer (10^{15} molecules).

From the left panel of Figure 1, there is a substantial gap between the signals from the 2 minute and 5 minute experiments (see Appendix), so the transition from multilayer dominated to submonolayer dominated regimes is not completely clear. However, for our purposes, the integrated area corresponding to one monolayer should be accurate to within a factor of 2.

4 Description of Experiments

Table 4: Experiments discussed in this thesis. The number of monolayers for each experiment is based on IR measurements (see Section 3.2). Temperature measurements have an uncertainty of 2 K, monolayer film thicknesses uncertainties of at least 30 %, and UV lamp fluxes have uncertainties of approximately 10 %.

Experiment Number	Irradiation Time (hr)	Temperature (K)	Monolayers	UV Lamp Flux ($\times 10^{13}$) (Photons Second^{-1})
1	0.5	20	239	5.44
2	1	20	198	5.16
3	1	20	198	7.97
4	2	20	204	5.92
5	2	20	230	5.95
6	2	20	223	8.28
7	4	20	216	4.91
8	4	20	215	5.44
9	4	20	231	5.57
10	6	20	205	5.52
11	6	20	170	3.32
12	6	20	193	6.14
13	8	20	188	5.95
14	8	20	213	6.70
15	4	15	189	5.85
16	4	25	199	4.64
17	4	25	186	6.19
18	4	50	203	8.77

All CO_2 photolysis experiments used to constrain O_2 photoproduction in this thesis are listed in

Table 4. Experiment 7 is used as the fiducial experiment. Experiments 1-14, with different irradiation times at a constant temperature of 20 K, are used to explore the relationship between O_2 formation and UV photon fluence. Experiments 15-18, in addition to Experiments 7-9, are used to compare O_2 formation efficiencies at different temperatures for a four hour irradiation.

5 O_2 Production: Proof of Concept

Evidence of O_2 formation is given in a sample TPD result shown in Figure 2. This O_2 signal, as with all the O_2 areas and signals throughout this thesis, has been corrected for O_3 fractionation in the QMS. All experiments show evidence of O_2 generation for studies of both O_2 formation as a function of fluence (Figure 3) and of O_2 formation at different ice temperatures (Figure 4).

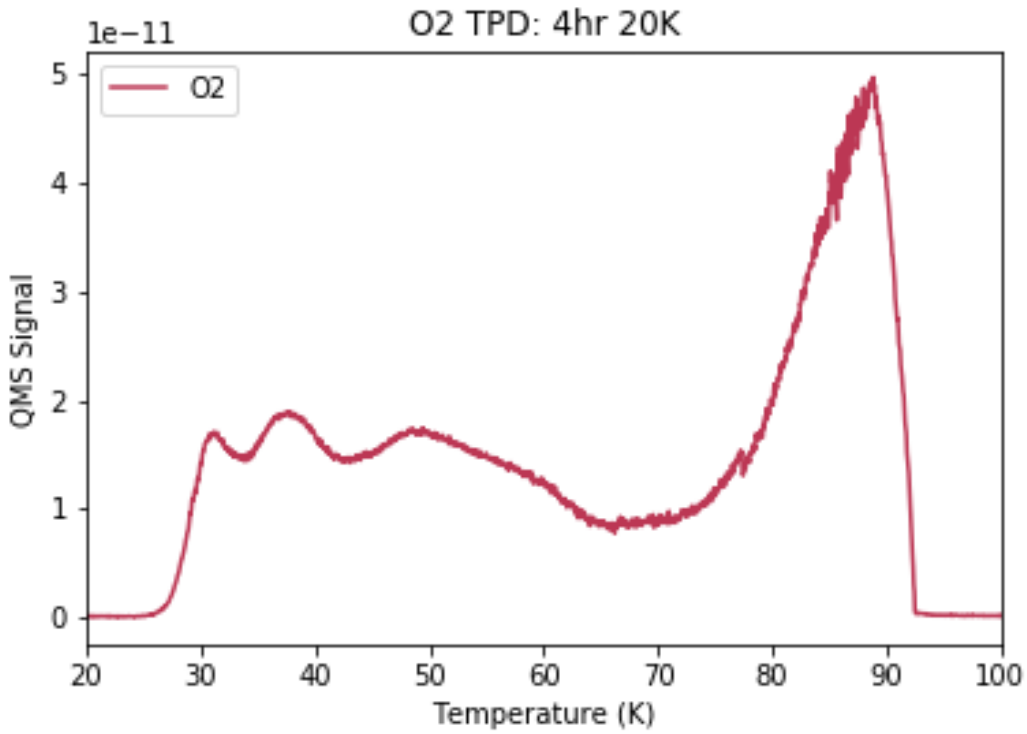

Figure 2: Temperature Programmed Desorption signal of O_2 ($m/z = 32$) from Experiment 7: 4 hour irradiation with an ice temperature of 20 K.

O_2 starts desorbing at 25 K, with the largest feature at around 90 K. This high temperature feature corresponds to the largest CO_2 desorption peak, and no significant amounts of other molecules with $m/z = 32$ are present in the chamber. For a TPD spectrum with all monitored m/z signals, see the supplemental figures.

Figure 5 shows the second piece of evidence of O_2 formation: a growing O_3 IR spectral band during irradiation of the fiducial ice (Experiment 7).

However, the QMS signal varied in an unpredictable way between experiments, preventing direct O_2 TPD comparisons between them. For detailed analysis of this problem and troubleshooting attempts, see the appendix.

Because we cannot at this moment use the O_2 TPD signals to constrain O_2 production yields, we instead use IR measurements of CO and O_3 production in the next section to determine upper and lower bounds for O_2 production.

6 Constraints on O_2 Yields: CO and O_3 Formation

In light of the inconsistencies of the TPD results, an examination of CO and O_3 IR features may provide a more accurate basis for comparison between different experiments.

CO must form before O_2, and O_2 is a precursor to O_3 formation. Within the CO_2 ice, these photoproducts form through a series of reactions, which we find to be in agreement with the reaction network previously proposed by Martín-Doménech et al (2015) [36]:

$$CO_2 + h\nu \rightarrow CO + O \tag{7}$$

$$O + O \rightarrow O_2 \tag{8}$$

$$O_2 + O \rightarrow O_3 \tag{9}$$

The above reactions are likely the dominant formation mechanisms at small fluences, when UV photons are far more likely to interact with CO_2 than any other molecule due to relative abundances.

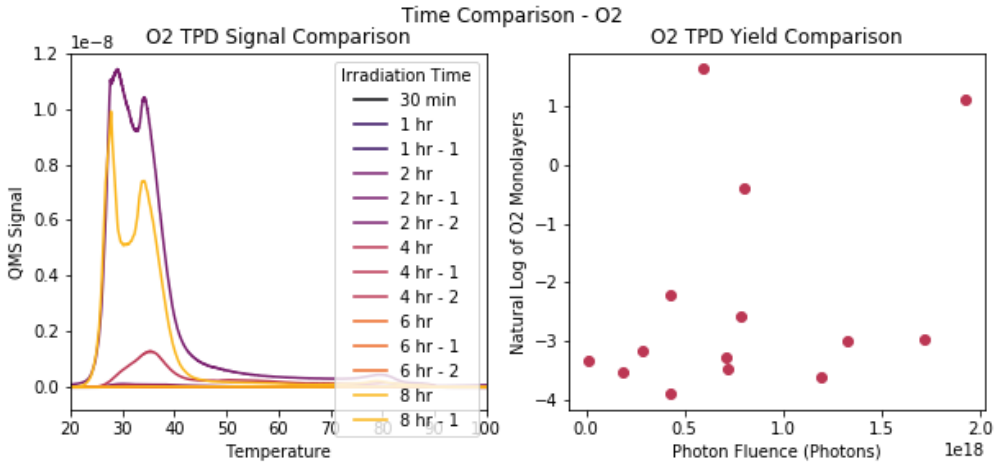

Figure 3: O_2 TPD data as a function of fluence, collected from different experiments. Left: the QMS signal for Experiments 1-14 as a function of temperature. Right: The total number of O_2 monolayers produced as a function of fluence. The suspiciously low yield for most of the experiments, in addition to the presence of the three outliers (experiments 6, 9, and 14), is indicative of a QMS problem - see Appendix.

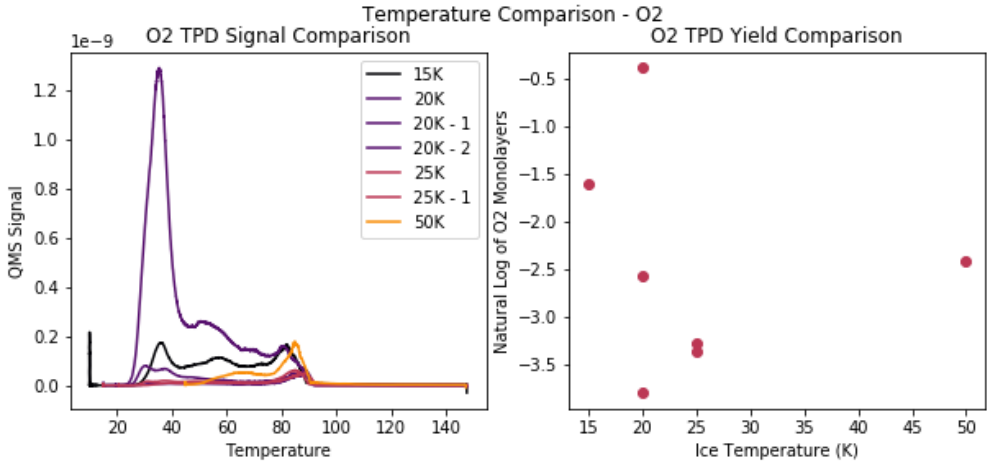

Figure 4: O_2 TPD data as a function of ice temperature following 4 hours of UV irradiation. Left: the QMS signal for Experiments 7-9 and 15-18 as a function of temperature. Right: The total number of O_2 monolayers produced from ices at different temperatures.

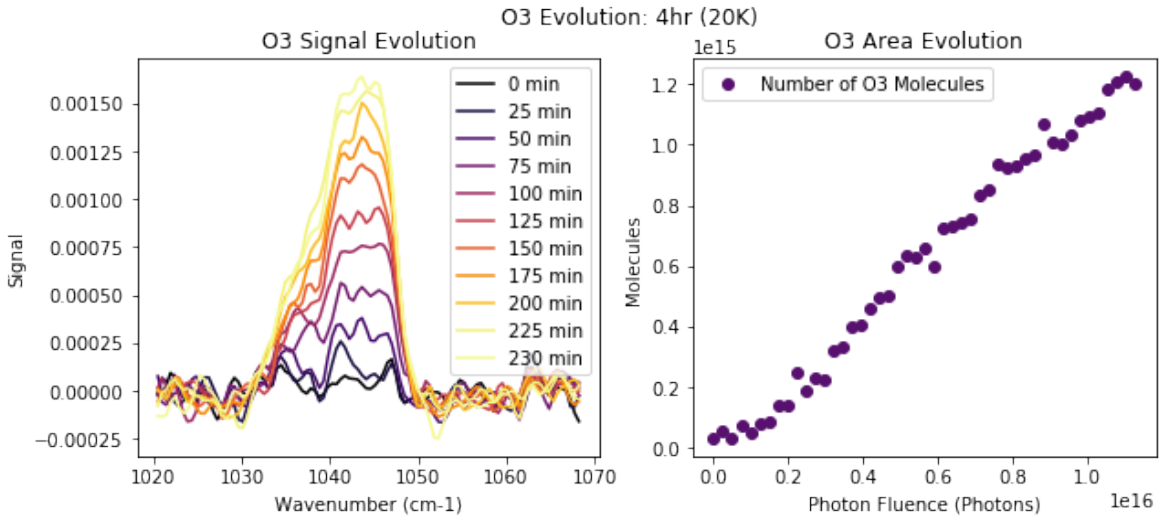

Figure 5: Evolution of the O_3 feature at 1040 cm^{-1} over the course of a 4 hour irradiation (Experiment 7). Left: IR signals measured at different times, with increasing brightness corresponding to increasing fluence. Right: the integrated area of this feature in number of molecules of O_3 formed as a function of photon fluence.

However, photodissociation pathways for O_2 and O_3 also exist:

$$O_2 + h\nu \rightarrow O + O \tag{10}$$

$$O_3 + h\nu \rightarrow O_2 + O \tag{11}$$

These destructive mechanisms become increasingly relevant at large fluences, as the relative amounts of species other than CO_2 grow. As these dissociative mechanisms become more important, photoproduct formation slows and no longer resembles a linear regime. However, the relative amounts of photoproducts will likely not change significantly. Based on the order of the primary formation mechanisms, we can predict a rudimentary estimate for the relative yields of each photoproduct. The single step CO mechanism should result in the most production, while the more complicated O_3 formation pathway would cause O_3 to be the least abundant species. O_2, our molecule of interest, would have an estimated yield somewhere between that of its precursor, CO, and that of the dependent species O_3.

Figure 6 shows CO (yellow) and O_3 (purple) IR yields as a function of photon fluence and at

different ice temperatures.

CO sublimates at ≈ 25 K, so at temperatures below 25 K, we assume that loss of photoproducts from the ice is minimal. With the additional assumption that CO, O_2, and O_3 are the main products of CO_2 photolysis, we apply a mass balance argument to estimate the amount of O_2 formed:

$$N_{O_2} \approx \frac{N_{CO} - 3 \times N_{O_3}}{2} \tag{12}$$

This estimation method is based off of the number of O atoms present in each species. At higher ice temperatures ($T \geq 25$ K), CO begins to desorb, and this estimation method cannot be used. The results from this approximation for the fluence series and low-temperature ices from the temperature series are shown in Figure 7.

For all experiments, this estimation suggests small amounts of O_2 formation, approximately equivalent to O_3 final yields of less than 2 ML at maximum.

7 O_2 Formation Mechanism: CO and O_3 Formation Kinetics

Figure 5 in the previous section showed the evolution of the O_3 feature during Experiment 7, a four hour UV irradiation at 20 K. Figure 8 shows a similar figure, showing evolution of the CO feature at its stretching band at 2141 cm^{-1} for the same experiment.

CO evolution starts almost immediately, which is to be expected from the reaction mechanisms given previously. It should be the first photoproduct to form, as it requires only the breaking of one C - O bond in CO_2 to form. O_3 evolution, on the other hand, requires three steps, and so does not begin immediately.

CO and O_3 IR evolution curves as a function of fluence for several fluence series experiments are overplotted in Figure 9. For clarity, only one experiment with each irradiation time is shown. In agreement with the results from the fiducial experiment (from figures 5 and 8), CO evolution begins immediately for all experiments, while O_3 evolution starts after a slight delay. Both photoproducts show a linear regime for small fluences followed by a leveling off of final amounts. For CO, the linear regime is most prominent for photon fluences of less than 0.5 $\times 10^{16}$ photons, and the leveling off starts

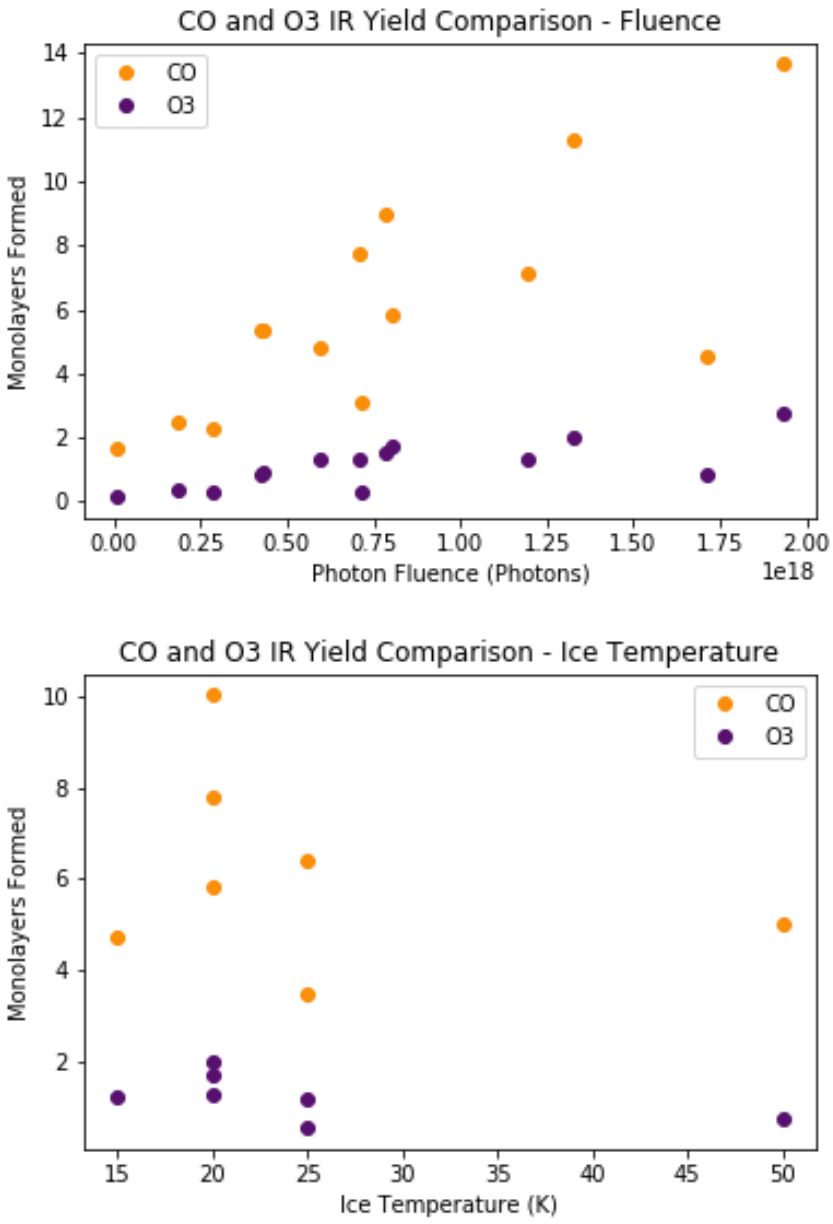

Figure 6: Top: CO and O_3 IR yields as a function of photon fluence, as taken from the final IR scan at the end of irradiation for Experiments 1-14, all at 20 K. Bottom: CO and O_3 IR yields at different ice temperatures, from the final IR scan at the end of the 4 hour irradiation for Experiment 7-9 and 15-18.

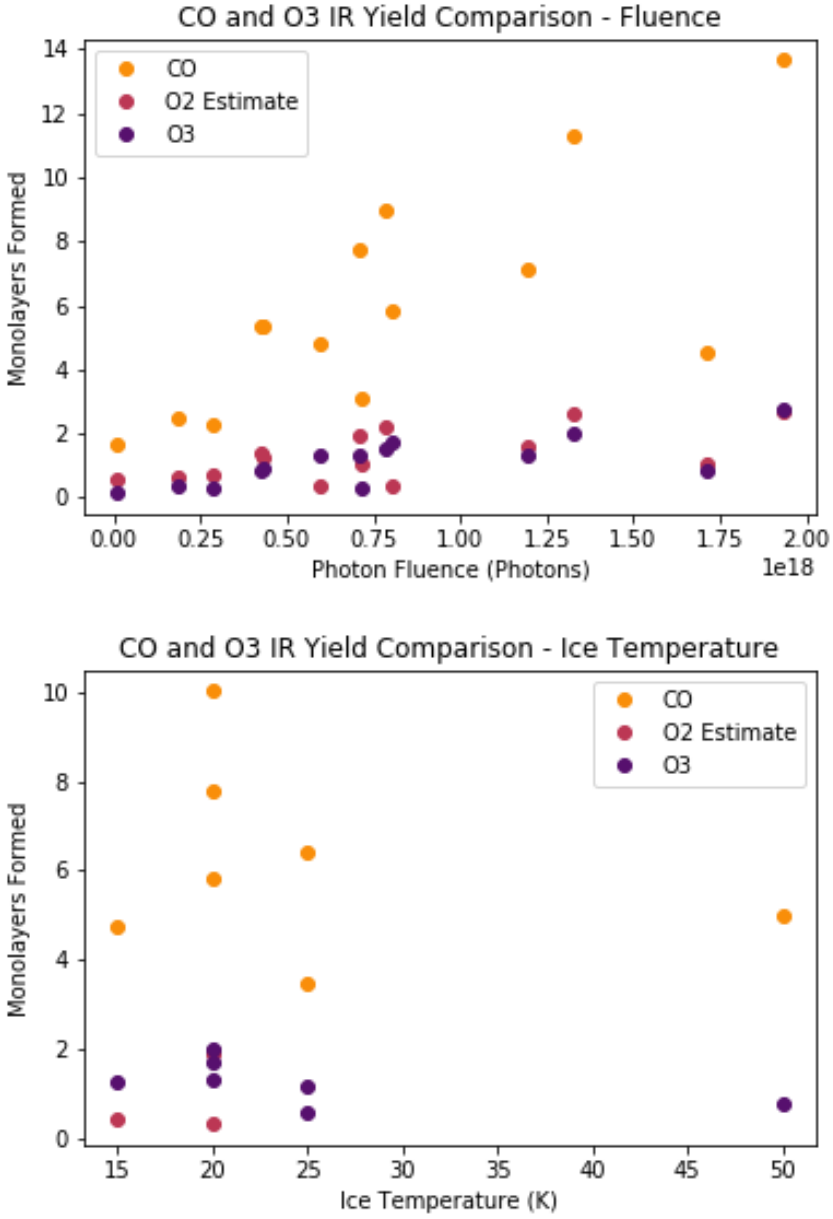

Figure 7: The same CO and O_3 results from Figure 6, overplot with the O_2 predicted yield from the mass balance estimation relationship (see text of Section 6). Top: CO IR, O_3 IR, and estimated O_2 yields as a function of fluence for Experiments 1-14. Bottom: CO IR, O_3 IR, and estimated O_2 yields at different ice temperatures, from the final IR scan at the end of irradiation for Experiments 7-9 and 15-18.

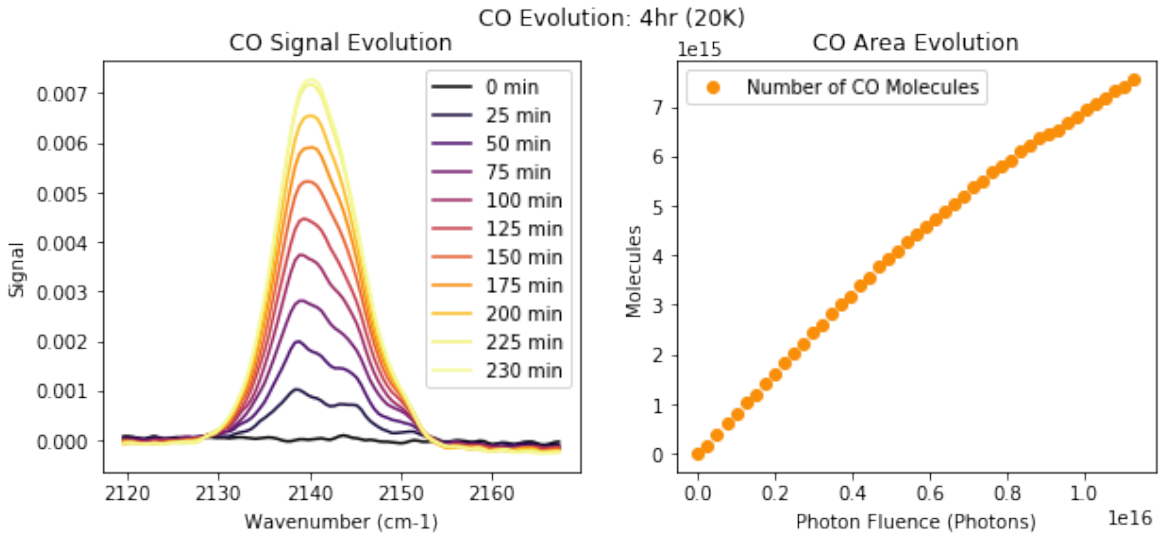

Figure 8: Evolution of the CO feature at 2141 cm^{-1} over the course of an 4 hour irradiation (Experiment 7). Left: the IR signal at different times, with increasing brightness corresponding to increasing fluence. Right: the integrated area of this feature in number of molecules as a function of photon fluence.

much earlier.

Operating under the assumption that O_2 formation follows a similarly shaped evolution pathway, we would anticipate the shift from linear regime to occur at a fluence between 0.5 and 1 $\times 10^{16}$ photons.

In terms of final yield as a function of fluence, the total number of monolayers of CO formed from Experiments 1-14 is shown in Figure 10. With the exception of a few outliers, the overall trend shows a similar distribution to the evolution curves in Figures 8 and 9: as fluence increases, the total amount of CO formed also increases. Net CO yield has not yet reached steady state conditions, but Figure 10 shows that after 8 hours of irradiation, the CO yield is roughly 14 ML, representing approximately 7 % of the original CO_2 ice.

As a comparison, Figure 11 shows the total number of monolayers of O_3 formed as a function of fluence (Experiments 1-14). Again, the yield of O_3 increases as a function of fluence, with rapid growth at smaller fluences slowing to less drastic increases at larger photon fluences. The tapering off at high fluences suggests that the yield approaches the maximum amount of O_3 possible to form from approximately 200 ML of CO_2. This maximum amount corresponds to about 2 ML, representing 1-2

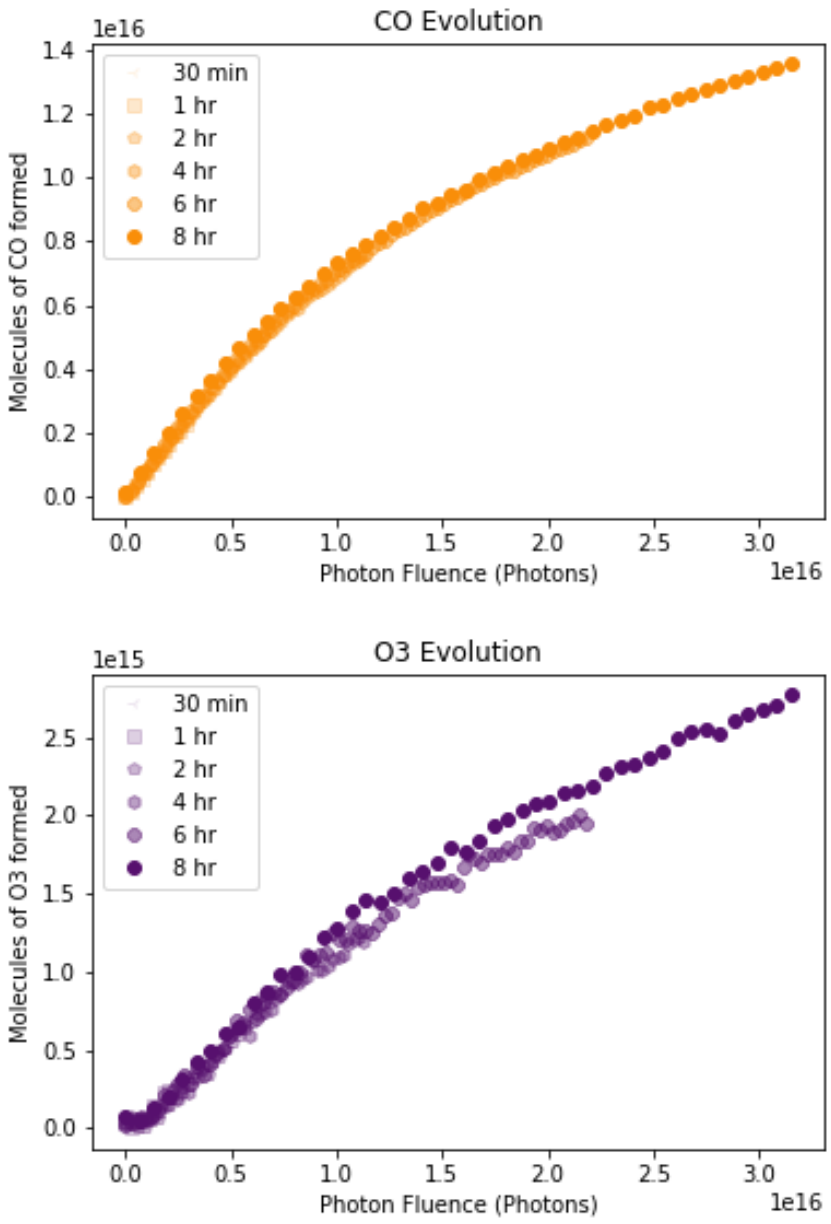

Figure 9: Evolution of CO (top) and O_3 (bottom) IR features within experiments 1, 2, 4, 7, 10, and 14 (one experiment per irradiation time). The ozone feature consistently features a delay before any formation is observed, then displays a linear regime followed by a leveling off. The carbon monoxide feature starts evolving as soon as irradiation begins, and reaches a linear regime earlier.

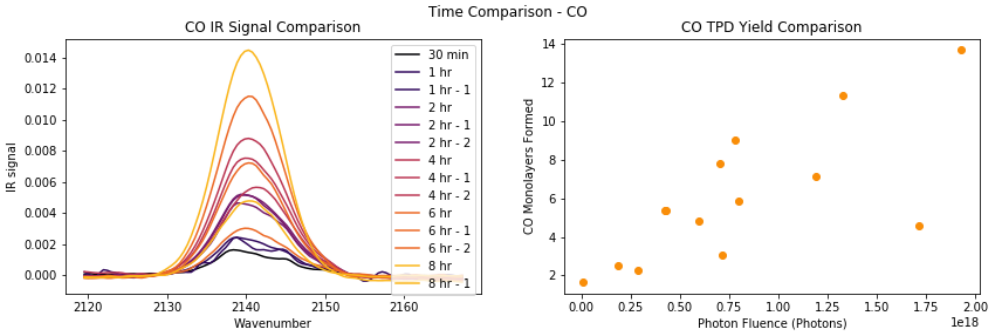

Figure 10: CO IR yield as a function of photon fluence from experiments 1-14 (20 K). Left: the final IR scan at the end of the irradiation for each experiment. Right: the natural log of the number of monolayers of CO formed. With a few outliers, the number of monolayers for these different experiments follows a linear regime for small fluences, followed by a tapering off. This matches the trend seen in Figure 9 for CO growth within an experiment.

% of the initial CO_2 ice.

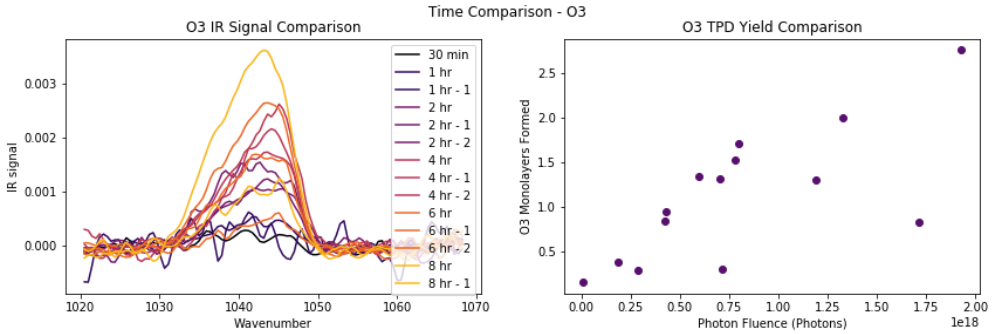

Figure 11: O_3 IR yield as a function of photon fluence from experiments 1-14 (20 K). Left: the final IR scan at the end of the irradiation for each experiment. Right: the natural log of the number of monolayers of O_3 formed. The linear regime followed by a leveling off matches the trend seen in Figure 9 for O_3 growth within an experiment.

The experiments at different temperatures also illustrate this same increase in CO and O_3 production as a function of fluence. The linear increase followed by a tapering off remains the same shape, but the slope of the linear increase depends on temperature. Figure 12 shows the O_3 and CO evolution curves for Experiments 7, 15, 17, and 18, corresponding to ice temperatures of 15 K, 20 K, 25 K, and 50 K, each for a 4 hour experiment.

CO formation shows a strong temperature dependence: the rate of formation is fastest at an ice

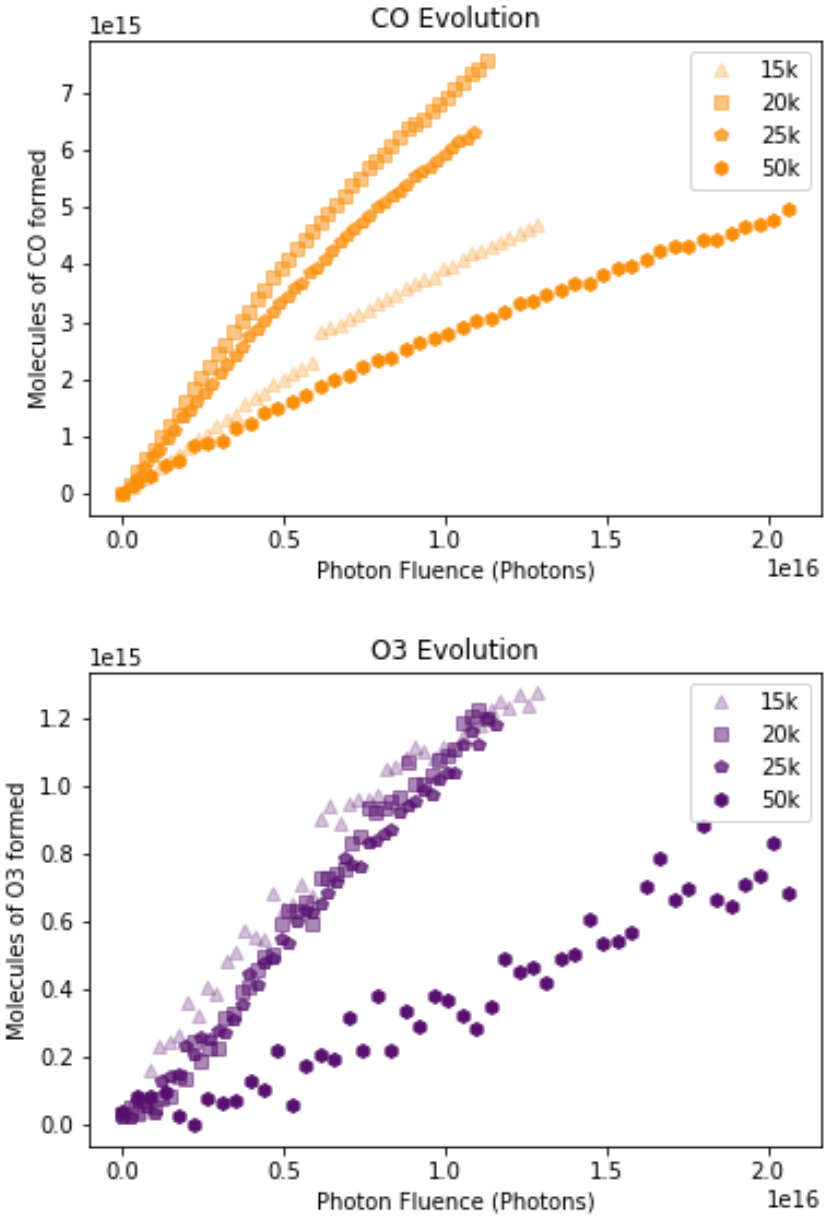

Figure 12: Evolution of CO (top) and O_3 (bottom) IR features as a function of fluence for Experiments 7 (20 K), 15 (15 K), 17 (25 K), and 18 (50 K), all for 4 hours of irradiation. All show a linear increase in photoproduct yield for small fluences followed by a gradual slowing of photoproduct formation. CO shows the fastest rate of increase at an ice temperature of 20 K, with 15 K and 25 K rates somewhat smaller. O_3 evolution at 20 K, 15 K, and 25 K show comparable rates of formation. Both photoproducts show the smallest rate of formation at an ice temperature of 50 K.

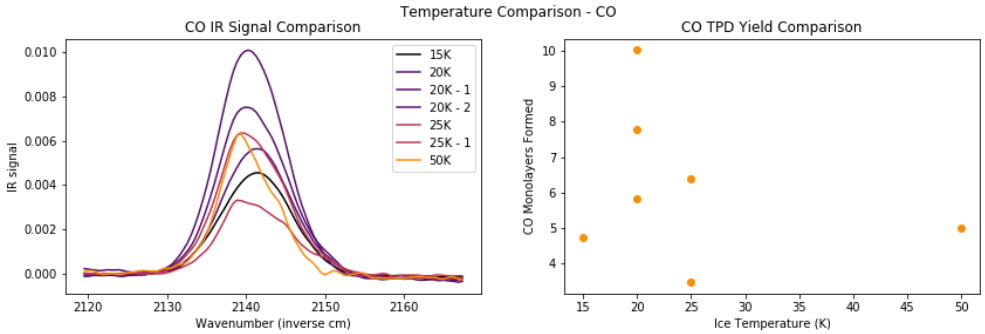

Figure 13: CO IR data as a function of ice temperature for Experiments 7-9 and 15-18. Left: the final IR scan at the end of the 4 hour irradiation for each experiment. Right: the natural log of the number of CO monolayers formed.

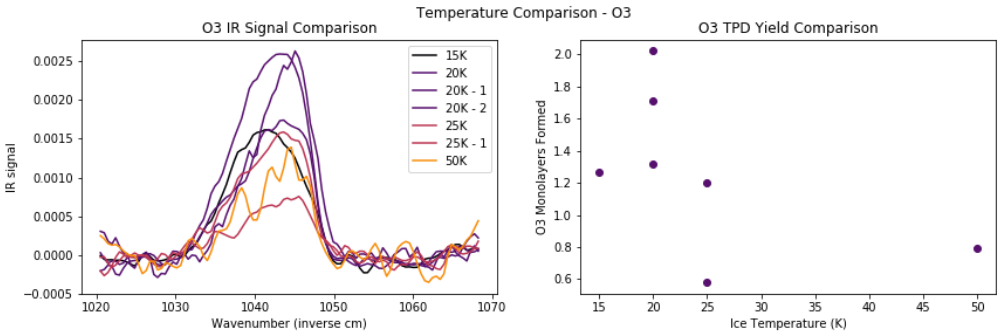

Figure 14: O_3 IR data as a function of ice temperature for Experiments 7-9 and 15-18. Left: the final IR scan at the end of the 4 hour irradiation for each experiment. Right: the natural log of the number of O_3 monolayers formed.

temperature of 20 K, and the total amount of CO is the greatest at approximately 7 monolayers. At all other ice temperatures, the slope of the growth curve is smaller, with the 50 K growth curve the smallest. The 25 K evolution is more similar to the evolution at 20 K, while the 15 K evolution is more similar to the 50 K experiment in terms of slope. All growth curves show CO evolution starting immediately, even at low fluences.

The three smaller temperatures show comparable rates of O_3 evolution, with similar slopes for the growth curve and approximately the same number of monolayers formed: roughly 1 monolayer. Like the CO growth curves, the 50 K O_3 evolution has the least steep slope and the smallest amount of final photoproduct formed. At all temperatures, O_3 evolution does not start immediately but instead

has a delay before any production is observed.

For more direct comparison between photoproduct yields at different temperatures, Figure 13 shows final IR signals and CO photoproduct yields and Figure 14 shows the same for O_3. Figure 13 shows that the number of monolayers of CO is between 4 and 10, with the maximum amount of CO formation at 20 K.

The maximum amount of O_3 formed is at an ice temperature of 20 K, though O_3 yield at 15 K, 20 K, and 25 K does not vary as much as CO yield does. The total O_3 yield is between half a monolayer and two monolayers, so variation is not very large.

8 Discussion

8.1 Fluence and Photoproduct Formation

Assuming that the two step O_2 formation mechanism proposed at the beginning of Section 6 accurately reflects the dominant formation mechanisms of the photoproducts examined here, we would expect a final photoproduct relative abundance order of the most CO, a medium amount of O_2, and the smallest amount of O_3. Solely from the IR data, all experiments show more production of CO than O_3 by a factor of at least 3. The mass balance scheme showed in Section 6 suggests that this reaction scheme is reasonable. We then propose that O_2 formation growth curves and final yield fall somewhere between those of CO and O_3.

Because O_2 forms through a two step process, we would expect its formation as a function of fluence to have a delay. At very low fluences, not enough free O atoms have formed from CO_2 photolysis to allow for substantial O_2 production. This delay would be for a smaller time period than O_3, because there are fewer steps in the formation mechanism. Following the delay, we would expect O_2 growth curves to first have a linear regime that slowly tapers off to a steady concentration. The fluence required to leave the linear regime should be between that of CO and O_3, for an estimated value between 0.5 and 1 $\times 10^{16}$ photons.

The estimated yield for the final amount of O_2 would also fall between that of CO and O_3. For photolysis of approximately 200 ML of CO_2, the maximum amount of CO formed appears to be about

14 ML (Figures 9 and 10), while the maximum amount of O_3 is about 2.5 ML (Figures 9 and 11). This suggests that the amount of O_2 formed is approximately between 3 ML and 7 ML. This represents 1.5 % to 7 % of the original CO_2 ice.

8.2 Temperature and Photoproduct Formation

Interpretation of O_2 formation at different temperatures is made slightly more uncertain by the differences in CO and O_3 growth curves (Figure 12). O_3 evolution at 15, 20, and 25 K seems to be comparable, while CO evolution shows more of a difference in these growth curves. O_2 could potentially follow either trend, depending on the temperature dependence of O atom combination. If O_2 follows a CO-like trend and has differences in growth curves for 15 K, 20 K, and 25 K, then the fact that O_3 does not significantly vary would suggest that the reaction of O and O_2 to form O_3 is temperature-independent over this temperature range. If O_2 growth curves are instead more similar to O_3 and are comparable over this temperature range, then the combination of O atoms to form O_2 would be temperature-independent instead.

Because of this ambiguity, the temperature with the maximum amount of O_2 yield is uncertain. Based on the CO and O_3 maximums, O_2 likely has a maximum yield between 20 and 25 K. In either case, O_2 yield at 50 K is likely significantly smaller than at lower temperatures.

All photoproducts monitored show the smallest amount of formation at 50 K. The signal-to-noise ratio is not ideal within the IR spectrum (Figures 11 and 12), so the precise number of monolayers has some uncertainty associated with it, but the relative amount of both CO and O_3 formed is still smaller than at lower temperatures. This may be explained by looking at the temperatures where photoproducts start desorbing in the TPD data. From the CO and O_2 signals shown in Figure 18 (see Appendix), while the relative size of the peaks in the two experiments differ, both experiments show CO and O_2 desorption starting at temperatures below 30 K. At an ice temperature of 50 K, then, large quantities of photoproducts including CO and O_2 may be thermally desorbing from the ice during irradiation. Free oxygen atoms, which O_2 and O_3 formation depend on, may also desorb in greater numbers from 50 K ice than from colder ice. The resulting smaller amount of these species within the ice would then explain the lower observed formation.

9 Conclusions

Observations of CO_2 photolysis revealed the formation of O_2. It was detected both directly from TPD measurements following UV irradiation and indirectly from the presence and evolution of an IR feature corresponding to O_3, which forms from O_2. While QMS issues prevent accurate comparison of TPD data between experiments, upper and lower bounds of O_2 production can be given from IR measurements of CO and O_3 formation, respectively. Based on these mass balance estimates, O_2 yield increases as a function of fluence to a maximum relative abundance of between 1 - 7 % of the original amount of CO_2 dosed. The estimation methods used provide a reasonable estimate of the right order of magnitude of O_2 production, though likely on the low side. Comparisons with CO and O_3 formation as a function of temperature suggest that this maximum relative abundance at 20 K represents close to the maximum amount of O_2, as at higher temperatures, production of CO and O_3 decreases.

These findings suggest that O_2 does indeed form from CO_2 photolysis. The likely optimal conditions for its formation would be a high UV fluence and a CO_2 ice temperature of between 20 - 25 K. This temperature range is possible for interstellar ices, so this pathway could be responsible for some interstellar or cometary O_2, though other formation mechanisms seem likely required to produce O_2 in the observed abundances. Future experiments to better characterize O_2 formation yields and pathways would include both TPD and IR data to provide quantitative O_2 information. Additional future experiments would including monitoring of O_2 production from photolysis of mixed, isotopically labeled, CO_2 and H_2O ices to determine whether yields are larger or smaller than in single-species ice.

References

[1] K. Acharyya, G. W. Fuchs, H. J. Fraser, E. F. van Dishoeck, and H. Linnartz. Desorption of CO and O $_2$ interstellar ice analogs. *Astronomy & Astrophysics*, 466(3):1005–1012, May 2007.

[2] D. A. Bahr, M. Fam, R. A. Vidal, and R. A. Baragiola. Radiolysis of water ice in the outer solar system: Sputtering and trapping of radiation products. *Journal of Geophysical Research: Planets*, 106(E12):33285–33290, 2001.

[3] E. S. Barker. Detection of Molecular Oxygen in the Martian Atmosphere. *Nature*, 238(5365):447–448, August 1972.

[4] Jennifer B. Bergner, Karin I. berg, and Mahesh Rajappan. Methanol Formation via Oxygen Insertion Chemistry in Ices. *The Astrophysical Journal*, 845(1):29, August 2017.

[5] A. Bieler, K. Altwegg, H. Balsiger, A. Bar-Nun, J.-J. Berthelier, P. Bochsler, C. Briois, U. Calmonte, M. Combi, J. De Keyser, E. F. van Dishoeck, B. Fiethe, S. A. Fuselier, S. Gasc, T. I. Gombosi, K. C. Hansen, M. Hssig, A. Jckel, E. Kopp, A. Korth, L. Le Roy, U. Mall, R. Maggiolo, B. Marty, O. Mousis, T. Owen, H. Rme, M. Rubin, T. Smon, C.-Y. Tzou, J. H. Waite, C. Walsh, and P. Wurz. Abundant molecular oxygen in the coma of comet 67p/ChuryumovGerasimenko. *Nature*, 526(7575):678–681, October 2015.

[6] Jrgen Blum, Bastian Gundlach, Steffen Mhle, and Josep M. Trigo-Rodriguez. Comets formed in solar-nebula instabilities! – An experimental and modeling attempt to relate the activity of comets to their formation process (corrigendum included). *Icarus*, 235:156–169, June 2014. arXiv: 1403.2610.

[7] Arthur Bosman, Simon Bruderer, and Ewine F. van Dishoeck. CO2 infrared emission as a diagnostic of planet-forming regions of disks. *Astronomy & Astrophysics*, 601:A36, May 2017. arXiv: 1701.08040.

[8] Alexis Bouquet, Olivier Mousis, Benjamin Teolis, Georgios Nicolaou, Ozge Ozgurel, Francoise Pauzat, Yves Ellinger, Thomas Ronnet, and J. Hunter Waite. Limits on the Contribution of Endogenic Radiolysis to the Presence of Molecular Oxygen in Comet 67p/ChuryumovGerasimenko. *The Astrophysical Journal*, 864(1):9, August 2018.

[9] G. Cessateur, J. De Keyser, R. Maggiolo, A. Gibbons, G. Gronoff, H. Gunell, F. Dhooghe, J. Loreau, N. Vaeck, K. Altwegg, A. Bieler, C. Briois, U. Calmonte, M. R. Combi, B. Fiethe, S. A. Fuselier, T. I. Gombosi, M. Hssig, L. Le Roy, E. Neefs, M. Rubin, and T. Smon. Photochemistry of forbidden oxygen lines in the inner coma of 67p/Churyumov-Gerasimenko. *Journal of Geophysical Research: Space Physics*, 121(1):804–816, 2016.

[10] Jo-Hsin Chen, Paul F. Goldsmith, Serena Viti, Ronald Snell, Dariusz C. Lis, Arnold Benz, Edwin Bergin, John Black, Paola Caselli, Pierre Encrenaz, Edith Falgarone, Javier R. Goicoechea, ke Hjalmarson, David Hollenbach, Michael Kaufman, Gary Melnick, David Neufeld, Laurent Pagani, Floris van der Tak, Ewine van Dishoeck, and Umut A. Yldz. *HERSCHEL* HIFI OBSERVATIONS OF O $_2$ TOWARD ORION: SPECIAL CONDITIONS FOR SHOCK ENHANCED EMISSION. *The Astrophysical Journal*, 793(2):111, September 2014.

[11] F. Combes, T. Wiklind, N. Nakai, Paris Observatory, Onsala Observatory, and Nobeyama Observatory. New upper limits on the interstellar O2 abundance. *arXiv:astro-ph/9709026*, September 1997. arXiv: astro-ph/9709026.

[12] Th de Graauw, DCB Whittet, PA+ 2a Gerakines, OH Bauer, DA Beintema, ACA Boogert, DR Boxhoorn, JE Chiar, P Ehrenfreund, H Feuchtgruber, and others. SWS observations of solid CO2 in molecular clouds. *Astronomy and Astrophysics*, 1996.

[13] F. Dulieu, M. Minissale, and D. Bockele-Morvan. Production of O $_2$ through dismutation of H $_2$ O $_2$ during water ice desorption: a key to understanding comet O $_2$ abundances. *Astronomy & Astrophysics*, 597:A56, January 2017.

[14] P Ehrenfreund, R Breukers, LB d'Hendecourt, JM Greenberg, and others. On the possibility of detecting solid O2 in interstellar grain mantles. *Astronomy and Astrophysics*, 260:431, 1992.

[15] Christian Eistrup and Catherine Walsh. Formation of cometary O $_2$ ice and related ice species on grain surfaces in the midplane of the pre-solar nebula. *Astronomy & Astrophysics*, 621:A75, January 2019.

[16] R. M. Escribano, G. M. Munoz Caro, G. A. Cruz-Diaz, Y. Rodriguez-Lazcano, and B. Mate. Crystallization of CO2 ice and the absence of amorphous CO2 ice in space. *Proceedings of the National Academy of Sciences*, 110(32):12899–12904, August 2013.

[17] Edith C. Fayolle, Jodi Balfe, Ryan Loomis, Jennifer Bergner, Dawn Graninger, Mahesh Rajappan, and Karin I. berg. N $_2$ AND CO DESORPTION ENERGIES FROM WATER ICE. *The Astrophysical Journal*, 816(2):L28, January 2016.

[18] Katia M. Ferrire. The interstellar environment of our galaxy. *Reviews of Modern Physics*, 73(4):1031–1066, December 2001.

[19] Jonathan P. Gardner, John C. Mather, Mark Clampin, Rene Doyon, Matthew A. Greenhouse, Heidi B. Hammel, John B. Hutchings, Peter Jakobsen, Simon J. Lilly, Knox S. Long, Jonathan I. Lunine, Mark J. Mccaughrean, Matt Mountain, John Nella, George H. Rieke, Marcia J. Rieke, Hans-Walter Rix, Eric P. Smith, George Sonneborn, Massimo Stiavelli, H. S. Stockman, Rogier A. Windhorst, and Gillian S. Wright. The James Webb Space Telescope. *Space Science Reviews*, 123(4):485–606, November 2006.

[20] E. L. Gibb, D. C. B. Whittet, A. C. A. Boogert, and A. G. G. M. Tielens. Interstellar Ice: The *Infrared Space Observatory* Legacy. *The Astrophysical Journal Supplement Series*, 151(1):35–73, March 2004.

[21] Paul F. Goldsmith, Ren Liseau, Tom A. Bell, John H. Black, Jo-Hsin Chen, David Hollenbach, Michael J. Kaufman, Di Li, Dariusz C. Lis, Gary Melnick, David Neufeld, Laurent Pagani, Ronald Snell, Arnold O. Benz, Edwin Bergin, Simon Bruderer, Paola Caselli, Emmanuel Caux, Pierre Encrenaz, Edith Falgarone, Maryvonne Gerin, Javier R. Goicoechea, ke Hjalmarson, Bengt Larsson, Jacques Le Bourlot, Franck Le Petit, Massimo De Luca, Zsofia Nagy, Evelyne Roueff, Aage Sandqvist, Floris van der Tak, Ewine F. van Dishoeck, Charlotte Vastel, Serena Viti, and Umut Yldz. *HERSCHEL* MEASUREMENTS OF MOLECULAR OXYGEN IN ORION. *The Astrophysical Journal*, 737(2):96, August 2011.

[22] D. T. Hall, D. F. Strobel, P. D. Feldman, M. A. McGrath, and H. A. Weaver. Detection of an oxygen atmosphere on Jupiter's moon Europa. *Nature*, 373:677, February 1995.

[23] Eric Herbst and William Klemperer. The Formation and Depletion of Molecules in Dense Interstellar Clouds. *The Astrophysical Journal*, 185:505, October 1973.

[24] K. L. Heritier, K. Altwegg, J.-J. Berthelier, A. Beth, C. M. Carr, J. De Keyser, A. I. Eriksson, S. A. Fuselier, M. Galand, T. I. Gombosi, P. Henri, F. L. Johansson, H. Nilsson, M. Rubin, C. Simon Wedlund, M. G. G. T. Taylor, and E Vigren. On the origin of molecular oxygen in cometary comae. *Nature Communications*, 9(1), December 2018.

[25] J. D. Hunter. Matplotlib: A 2d graphics environment. *Computing In Science & Engineering*, 9(3):90–95, 2007.

[26] WILLIAM M Irvine, F PETER Schloerb, JACQUES Crovisier, BRUCE Fegley Jr, and MICHAEL J Mumma. Comets: A link between interstellar and nebular chemistry. *Protostars and planets IV*, 1159, 2000.

[27] Anders Johansen, Jeffrey S. Oishi, Mordecai-Mark Mac Low, Hubert Klahr, Thomas Henning, and Andrew Youdin. Rapid planetesimal formation in turbulent circumstellar disks. *Nature*, 448(7157):1022–1025, August 2007.

[28] R.E. Johnson, J.G. Luhmann, R.L. Tokar, M. Bouhram, J.J. Berthelier, E.C. Sittler, J.F. Cooper, T.W. Hill, H.T. Smith, M. Michael, M. Liu, F.J. Crary, and D.T. Young. Production, ionization and redistribution of O2 in Saturn's ring atmosphere. *Icarus*, 180(2):393–402, February 2006.

[29] Brian A. Keeney, S. Alan Stern, Michael F. AHearn, Jean-Loup Bertaux, Lori M. Feaga, Paul D. Feldman, Richard A. Medina, Joel Wm. Parker, Jon P. Pineau, Eric Schindhelm, Andrew J. Steffl, M. Versteeg, and Harold A. Weaver. H2o and O2 absorption in the coma of comet 67p/ChuryumovGerasimenko measured by the Alice far-ultraviolet spectrograph on Rosetta. *Monthly Notices of the Royal Astronomical Society*, 469(Suppl_2):S158–S177, July 2017.

[30] F. Lahuis, E. F. van Dishoeck, A. C. A. Boogert, K. M. Pontoppidan, G. A. Blake, C. P. Dullemond, N. J. Evans II, M. R. Hogerheijde, J. K. Jrgensen, J. E. Kessler-Silacci, and C. Knez. Hot Organic Molecules toward a Young Low-Mass Star: A Look at Inner Disk Chemistry. *The Astrophysical Journal*, 636(2):L145–L148, January 2006.

[31] B. Larsson, R. Liseau, L. Pagani, P. Bergman, P. Bernath, N. Biver, J. H. Black, R. S. Booth, V. Buat, J. Crovisier, C. L. Curry, M. Dahlgren, P. J. Encrenaz, E. Falgarone, P. A. Feldman, M. Fich, H. G. Florn, M. Fredrixon, U. Frisk, G. F. Gahm, M. Gerin, M. Hagstrm, J. Harju, T. Hasegawa, . Hjalmarson, L. E. B. Johansson, K. Justtanont, A. Klotz, E. Kyrl, S. Kwok, A. Lecacheux, T. Liljestrm, E. J. Llewellyn, S. Lundin, G. Mgie, G. F. Mitchell, D. Murtagh, L. H. Nordh, L.-. Nyman, M. Olberg, A. O. H. Olofsson, G. Olofsson, H. Olofsson, G. Persson, R. Plume, H. Rickman, I. Ristorcelli, G. Rydbeck, A. A. Sandqvist, F. V. Schele, G. Serra, S. Torchinsky, N. F. Tothill, K. Volk, T. Wiklind, C. D. Wilson, A. Winnberg, and G. Witt. Molecular oxygen in the Ophiuchi cloud. *Astronomy & Astrophysics*, 466(3):999–1003, May 2007.

[32] Trish Lauck, Leendertjan Karssemeijer, Katherine Shulenberger, Mahesh Rajappan, Karin I. berg, and Herma M. Cuppen. CO DIFFUSION INTO AMORPHOUS H $_2$ O ICES. *The Astrophysical Journal*, 801(2):118, March 2015.

[33] R. Liseau, P. F. Goldsmith, B. Larsson, L. Pagani, P. Bergman, J. Le Bourlot, T. A. Bell, A. O. Benz, E. A. Bergin, P. Bjerkeli, J. H. Black, S. Bruderer, P. Caselli, E. Caux, J.-H. Chen, M. de Luca, P. Encrenaz, E. Falgarone, M. Gerin, J. R. Goicoechea, . Hjalmarson, D. J. Hollenbach, K. Justtanont, M. J. Kaufman, F. Le Petit, D. Li, D. C. Lis, G. J. Melnick, Z. Nagy, A. O. H. Olofsson, G. Olofsson, E. Roueff, Aa. Sandqvist, R. L. Snell, F. F. S. van der Tak, E. F. van Dishoeck, C. Vastel, S. Viti, and U. A. Yldz. Multi-line detection of O $_2$ toward Ophiuchi A. *Astronomy & Astrophysics*, 541:A73, May 2012.

[34] Adrienn Luspay-Kuti, Olivier Mousis, Jonathan I. Lunine, Yves Ellinger, Franoise Pauzat, Ujjwal Raut, Alexis Bouquet, Kathleen E. Mandt, Romain Maggiolo, Thomas Ronnet, Bastien Brugger, Ozge Ozgurel, and Stephen A. Fuselier. Origin of Molecular Oxygen in Comets: Current Knowledge and Perspectives. *Space Science Reviews*, 214(8), December 2018.

[35] A. Lger, M. Fontecave, A. Labeyrie, B. Samuel, O. Demangeon, and D. Valencia. Is the Presence of Oxygen on an Exoplanet a Reliable Biosignature? *Astrobiology*, 11(4):335–341, May 2011.

[36] R. Martn-Domnech, J. Manzano-Santamara, G. M. Muoz Caro, G. A. Cruz-Daz, Y.-J. Chen, V. J. Herrero, and I. Tanarro. UV photoprocessing of CO $_2$ ice: a complete quantification of photochemistry and photon-induced desorption processes. *Astronomy & Astrophysics*, 584:A14, December 2015.

[37] Victoria S. Meadows, Christopher T. Reinhard, Giada N. Arney, Mary N. Parenteau, Edward W. Schwieterman, Shawn D. Domagal-Goldman, Andrew P. Lincowski, Karl R. Stapelfeldt, Heike Rauer, Shiladitya DasSarma, Siddharth Hegde, Norio Narita, Russell Deitrick, Jacob Lustig-Yaeger, Timothy W. Lyons, Nicholas Siegler, and J. Lee Grenfell. Exoplanet Biosignatures: Understanding Oxygen as a Biosignature in the Context of Its Environment. *Astrobiology*, 18(6):630–662, June 2018.

[38] O. Mousis, T. Ronnet, B. Brugger, O. Ozgurel, F. Pauzat, Y. Ellinger, R. Maggiolo, P. Wurz, P. Vernazza, J. I. Lunine, A. Luspay-Kuti, K. E. Mandt, K. Altwegg, A. Bieler, A. Markovits, and M. Rubin. ORIGIN OF MOLECULAR OXYGEN IN COMET 67p/CHURYUMOVGERASIMENKO. *The Astrophysical Journal*, 823(2):L41, June 2016.

[39] Michael J. Mumma and Steven B. Charnley. The Chemical Composition of CometsEmerging Taxonomies and Natal Heritage. *Annual Review of Astronomy and Astrophysics*, 49(1):471–524, 2011.

[40] K. S. Noll, T. L. Roush, D. P. Cruikshank, R. E. Johnson, and Y. J. Pendleton. Detection of ozone on Saturn's satellites Rhea and Dione. *Nature*, 388(6637):45–47, July 1997.

[41] Takafumi Ootsubo, Hideyo Kawakita, Saki Hamada, Hitomi Kobayashi, Mitsuru Yamaguchi, Fumihiko Usui, Takao Nakagawa, Munetaka Ueno, Masateru Ishiguro, Tomohiko Sekiguchi, Jun-ichi Watanabe, Itsuki Sakon, Takashi Shimonishi, and Takashi Onaka. *AKARI* NEAR-INFRARED SPECTROSCOPIC SURVEY FOR CO $_2$ IN 18 COMETS. *The Astrophysical Journal*, 752(1):15, June 2012.

[42] KlausM. Pontoppidan, A.C.A. Boogert, HelenJ. Fraser, EwineF. van Dishoeck, GeoffreyA. Blake, Fred Lahuis, KarinI. berg, NealJ. Evans II, and Colette Salyk. The c2d *Spitzer* Spectroscopic Survey of Ices around LowMass Young Stellar Objects. II. CO $_2$. *The Astrophysical Journal*, 678(2):1005–1031, May 2008.

[43] M. Rubin, K. Altwegg, E. F. van Dishoeck, and G. Schwehm. Molecular Oxygen in Oort Cloud Comet 1p/Halley. *The Astrophysical Journal Letters*, 815(1):L11, 2015.

[44] Nami Sakai, Takeshi Sakai, Yuri Aikawa, and Satoshi Yamamoto. DETECTION OF HCO2 TOWARD THE LOW-MASS PROTOSTAR IRAS 043682557 IN L1527. *The Astrophysical Journal*, 675:4, 2008.

[45] C. Salyk, K. M. Pontoppidan, G. A. Blake, J. R. Najita, and J. S. Carr. A *SPITZER* SURVEY OF MID-INFRARED MOLECULAR EMISSION FROM PROTOPLANETARY DISKS. II. CORRELATIONS AND LOCAL THERMAL EQUILIBRIUM MODELS. *The Astrophysical Journal*, 731(2):130, April 2011.

[46] S A Sandford and L J Allamandola. THE PHYSICAL AND INFRARED SPECTRAL PROPERTIES OF C02 IN ASTROPHYSICAL ICE ANALOGS. *ApJ. . .*, 355(1):16, 1990.

[47] M. T. Sieger, W. C. Simpson, and T. M. Orlando. Production of O2 on icy satellites by electronic excitation of low-temperature water ice. *Nature*, 394(6693):554–556, August 1998.

[48] Marco Spaans. THE ABUNDANCE AND EMISSION OF H2o AND O2 IN CLUMPY MOLECULAR CLOUDS. *The Astrophysical Journal*, 548:4, February 2001.

[49] John R. Spencer, Wendy M. Calvin, and Michael J. Person. Charge-coupled device spectra of the Galilean satellites: Molecular oxygen on Ganymede. *Journal of Geophysical Research: Planets*, 100(E9):19049–19056, 1995.

[50] V. Taquet, K. Furuya, C. Walsh, and E. F. van Dishoeck. A primordial origin for molecular oxygen in comets: a chemical kinetics study of the formation and survival of O $_2$ ice from clouds to discs. *Monthly Notices of the Royal Astronomical Society*, 462(Suppl 1):S99–S115, November 2016.

[51] B. D. Teolis, G. H. Jones, P. F. Miles, R. L. Tokar, B. A. Magee, J. H. Waite, E. Roussos, D. T. Young, F. J. Crary, A. J. Coates, R. E. Johnson, W.-L. Tseng, and R. A. Baragiola. Cassini Finds an Oxygen-Carbon Dioxide Atmosphere at Saturn's Icy Moon Rhea. *Science*, 330(6012):1813–1815, December 2010.

[52] AGGM Tielens, W Hagen, and others. Model calculations of the molecular composition of interstellar grain mantles. *Astronomy and Astrophysics*, 114:245, 1982.

[53] C. Vastel, C. Ceccarelli, B. Lefloch, and R. Bachiller. Abundance of HOCO $^+$ and CO $_2$ in the outer layers of the L1544 prestellar core. *Astronomy & Astrophysics*, 591:L2, July 2016.

[54] S.J. Weidenschilling. The Origin of Comets in the Solar Nebula: A Unified Model. *Icarus*, 127(2):290–306, June 1997.

[55] D. C. B. Whittet, S. S. Shenoy, E. A. Bergin, J. E. Chiar, P. A. Gerakines, E. L. Gibb, G. J. Melnick, and D. A. Neufeld. The Abundance of Carbon Dioxide Ice in the Quiescent Intracloud Medium. *The Astrophysical Journal*, 655(1):332–341, January 2007.

[56] Yunxi Yao and Konstantinos P. Giapis. Dynamic molecular oxygen production in cometary comae. *Nature Communications*, 8:15298, May 2017.

[57] Karin I. berg. Photochemistry and Astrochemistry: Photochemical Pathways to Interstellar Complex Organic Molecules. *Chemical Reviews*, 116(17):9631–9663, September 2016.

10 Appendix I: QMS Troubleshooting

All experiments show evidence of O_2 formation, but the distribution of O_2 yield is puzzling. We expect to see a steady increase in O_2 production with fluence. However, instead we see a small, near-constant amount of O_2 production (Figure 3) for the majority of experiments, and a few outliers with larger O_2 production.

Possible causes for this problem include overall QMS sensitivity variability, large actual differences in detection efficiency for different molecules, and vacuum chamber contamination. Based on ion counts during CO_2 dosing and O_2 dosing, contamination of $m/z = 44$ and $m/z = 32$ seem unlikely. Visible H_2O as a background signal is occasionally present, but because no CO_2 photolysis experiments involve the dosing of H_2O, we anticipate this to be a constant background signal. H_2O desorbs at higher temperatures than all other molecules monitored in CO_2 photolysis. If significant amounts of H_2O did accumulate on the crystal during irradiation and somehow trap the missing O_2, we would expect significant amounts of O_2 desorption at the same temperature as water during a TPD. This is not seen.

Variations within QMS signal for the same mass to charge ratio occurred even during the same day of experiments: all O_2 monolayer thickness data (Section 3.3, especially Table 3) were collected on the same day. Another experiment not listed, collected during the same day, was for a dose time of 4 minutes, but had an O_2 TPD signal in the 10^{-11} range, while the other experiments all had signals within the 10^{-9} range. Such a large discrepancy adds to the lack of reliability of comparing O_2 experiments to each other directly.

Returning to the CO_2 photolysis experiments, at small fluences, we expect a linear increase in O_2 production while the amount of O_2 is significantly smaller than the amount of CO_2. As the fluence increases, the final amount of O_2 should level off as reactions that consume O_2 become more prevalent. However, the majority of the the experiments seem to show significantly less than one monolayer of O_2 formed, with the yield remaining roughly constant. The few exceptions (experiments 6, 9, and 14) show several monolayers of O_2 formed.

However, evidence from the evolution of O_3 (Figures 4 and 6) suggests that O_2 yields of significantly less than one monolayer are unlikely, because the final amount of O_3 formed is approximately 1.2 monolayers in the fiducial experiment (Experiment 7), and O_3 is expected to form from O_2.

Another potential correction method is to compare the CO IR and TPD signals and determine a "scaling" factor to convert between molecules detected in the IR and TPD areas. Assuming that CO and O_2 have comparable QMS sensitivity, this conversion factor could be used to scale O_2 yields to reflect IR photoproduct amounts. These scaled O_2 yields are plotted in Figure 15, and still show very small yield. After scaling, all O_2 yields are within the range of 1 $\times 10^{10}$ molecules, five orders of magnitude smaller than one monolayer.

This is indicative of differences between CO and O_2 TPD signals: two sets of CO and O_2 signals are shown in Figure 17. These two sets are from Experiments 7 and 9, which have comparable parameters (4 hour irradiation, 20 K), and yet differ greatly. Experiment 7 shows very small O_2 yield relative to CO yield, while Experiment 9 shows less of a difference. A complete list of CO to O_2 TPD area ratios, and CO IR-to-TPD conversion factors, for all experiments can be found in Table 5.

In addition to differences in integrated area, the peak shapes in Figure 17 show very different features. For Experiment 7, which is indicative of most of the experiments, CO starts desorbing at around 25 K but has a larger at 85 K. O_2 also starts desorbing at this low temperature, but to a much smaller degree (see Figure 1 for a more detailed TPD signal). The large CO and O_2 feature at around 85 K is coincident with the main desorption peak of unreacted CO_2, suggesting that a significant

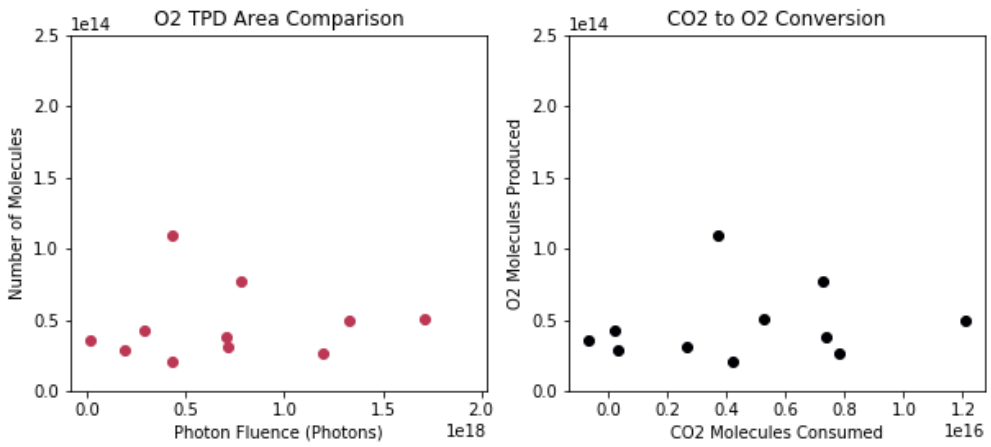

Figure 15: Left: O_2 production as a function of total fluence. Right: O_2 production as a function of CO_2 molecules consumed. The O_2 production is calculated from integrated TPD area of m/z 32, and O_2 area to molecules conversion factor is from O_2 TPDs (see Figure 1). The CO_2 molecules consumed is calculated from the difference in column densities in IR spectra (see Table 2 for band strengths). The average percent conversion from CO_2 to O_2 of the three outlying experiments (experiments 6, 9 and 14) is 67 %, while the average percent conversion of all other experiments is 2.7 %. The average percent conversion over all experiments is 16.5, because the three outliers are significantly higher.

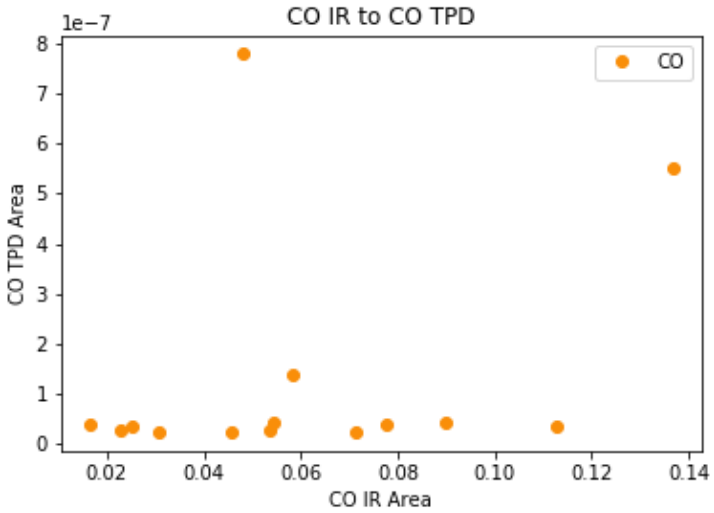

Figure 16: Ratio of CO IR area at the end of an irradiation vs CO area from a TPD plot for experiments 1-14.

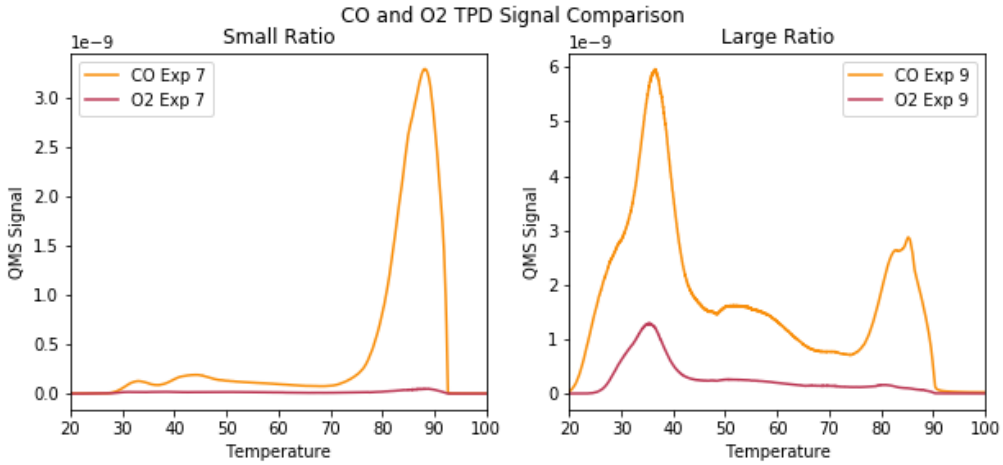

Figure 17: Two sets of CO and O_2 TPD signals, showing very different features. Left: CO and O_2 signals from experiment 7, which shows a very small O_2 peak relative to CO. Both species have a large peak at about 85 K, corresponding to species trapped in, and desorbing with, the CO_2 ice. Right: CO and O_2 signals from experiment 9, which shows a larger O_2 peak relative to CO. Both species have an additional feature at about 35 K. A complete list of CO to O_2 ratios for all experiments is found in Table 5.

Experiment Number	O_2 : CO TPD Area Ratio ($\times 10^{-2}$)	CO Conversion Factor
1	3	2.3×10^{-6}
2	3	1.3×10^{-6}
3	5	1.1×10^{-6}
4	2	5.1×10^{-7}
5	8	7.4×10^{-7}
6	20	1.6×10^{-5}
7	3	4.6×10^{-7}
8	6	4.5×10^{-7}
9	15	2.3×10^{-6}
10	4	3.2×10^{-7}
11	4	7.6×10^{-7}
12	4	3.0×10^{-7}
13	7	4.7×10^{-7}
14	16	4.0×10^{-6}
15	9	1.4×10^{-6}
16	3	5.6×10^{-7}
17	5	6.5×10^{-7}
18	9	5.8×10^{-7}

Table 5: O_2 to CO TPD area ratios and CO IR-TPD conversion factors. A two-order difference in conversion indicates a potentially major lack of stability in the QMS measurements.

amount of photoproducts are trapped within CO_2 ice layers.

In contrast, Experiment 9 shows stark differences in the the size of the low-temperature and high-temperature features relative to their sizes in Experiment 7. For both photoproducts, the feature at around 35 K is significantly larger than the 85 K feature. This seems to suggest that more photoproducts are on the surface than within the ice layers. For these comparable experiments, a difference this drastic is surprising.

Additionally, the variation in CO IR to TPD conversion factors appears to suggest that this QMS sensitivity issue may affect other masses besides *m/z 32* (Figure 16 and Table 5).

11 Supplemental Figures

Figure 18 shows all monitored mass to charge ratios (see Table 2) for the fiducial CO_2 TPD experiment (Experiment 7). Figure 19 shows the number of CO_2 molecules consumed as a function of photon fluence. All values in this figure are estimates, because these spectra are taken at an angle relative to the IR detector and column densities at angles are sensitive to impurities including photoproducts. This follows an overall linear trend: the greater the fluence, the more CO_2 molecules react. At very low fluences, ice re-structuring dominates the CO_2 signal. Figure 20 shows the O_3 IR to TPD conversion factors for all experiments.

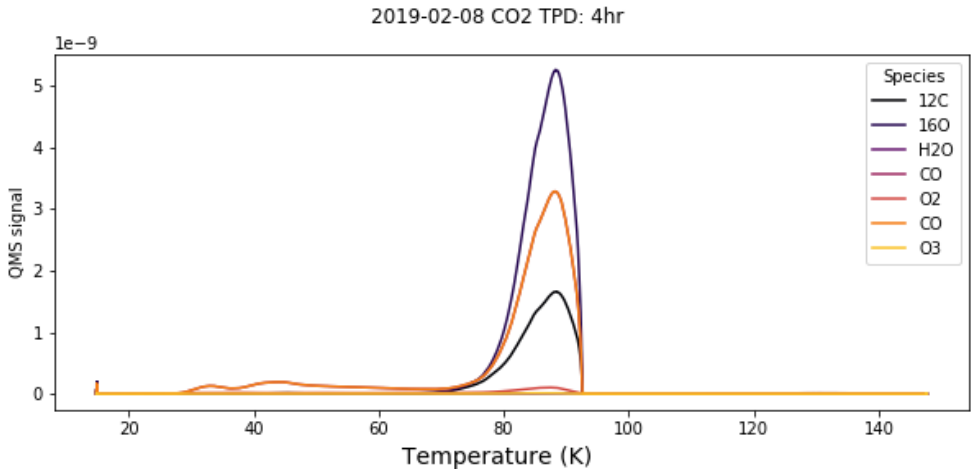

Figure 18: Temperature Programmed Desorption of all monitored fragments (see Table 2) following a 4 hour irradiation at 20 K (Experiment 7).

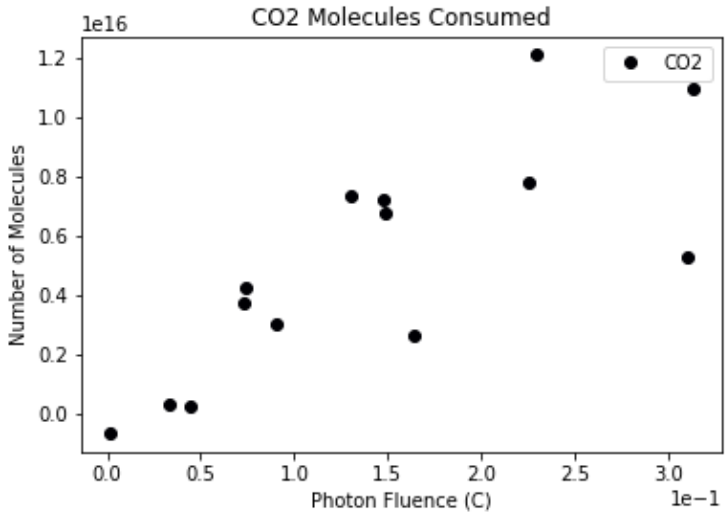

Figure 19: CO_2 molecules consumed as a function of fluence for Experiments 1-14, calculated from the difference in column densities in IR spectra taken at the beginning and end of UV irradiation.

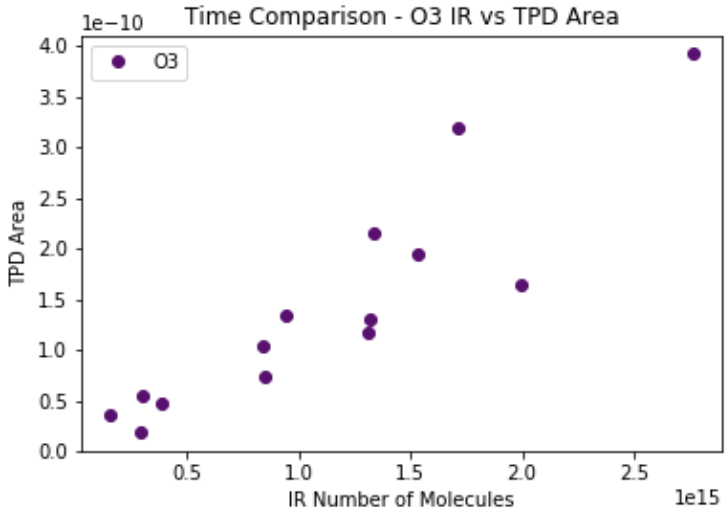

Figure 20: O_3 IR vs TPD areas for time series (Experiments 1-14).